applied sciences

MDPI

Article

A New Algorithm Model Based on Extended Kalman Filter for Predicting Inter-Well Connectivity

Liwen Guo [1], Zhihong Kang [1], Shuaiwei Ding [2], Xuehao Yuan [3], Haitong Yang [1], Meng Zhang [2] and Shuoliang Wang [1,*]

[1] School of Energy Resources, China University of Geosciences, Beijing 100083, China; guoliwenlw@163.com (L.G.); kangzh98@cugb.edu.cn (Z.K.); yhtgz1997@163.com (H.Y.)
[2] State Key Laboratory for Continental Dynamics, Department of Geology, Northwest University, Xi'an 710069, China; shwding@126.com (S.D.); 202323354@stumail.nwu.edu.cn (M.Z.)
[3] Department of Earth Science and Engineering, Imperial College London, London SW7 2AZ, UK; xuehao.yuan19@imperial.ac.uk
* Correspondence: wangshuoliang@cugb.edu.cn

Abstract: Given that more and more oil reservoirs are reaching the high water cut stage during water flooding, the construction of an advanced algorithmic model for identifying inter-well connectivity is crucial to improve oil recovery and extend the oilfield service life cycle. This study proposes a state variable-based dynamic capacitance (SV-DC) model that integrates artificial intelligence techniques with dynamic data and geological features to more accurately identify inter-well connectivity and its evolution. A comprehensive sensitivity analysis was performed on single-well pairs and multi-well groups regarding the permeability amplitude, the width of the high permeable channel, change, and lasting period of injection pressure. In addition, the production performance of multi-well groups, especially the development of ineffective circulation channels and their effects on reservoir development, are studied in-depth. The results show that higher permeability, wider permeable channels, and longer injection pressure maintenance can significantly enhance inter-well connectivity coefficients and reduce time-lag coefficients. Inter-well connectivity in multi-well systems is significantly affected by well-group configuration and inter-well interference effects. Based on the simulation results, the evaluation index of ineffective circulation channels is proposed and applied to dozens of well groups. These identified ineffective circulation channel changing patterns provide an important basis for optimizing oil fields' injection and production strategies through data-driven insights and contribute to improving oil recovery. The integration of artificial intelligence enhances the ability to analyze complex datasets, allowing for more precise adjustments in field operations. This paper's research ideas and findings can be confidently extended to other engineering scenarios, such as geothermal development and carbon dioxide storage, where AI-based models can further refine and optimize resource management and operational strategies.

Keywords: inter-well connectivity; multi-well system; ineffective circulation channels; extended Kalman filter; reservoir simulation

check for updates

Citation: Guo, L.; Kang, Z.; Ding, S.; Yuan, X.; Yang, H.; Zhang, M.; Wang, S. A New Algorithm Model Based on Extended Kalman Filter for Predicting Inter-Well Connectivity. *Appl. Sci.* **2024**, *14*, 9913. https://doi.org/10.3390/app14219913

Academic Editor: Luis Javier Garcia Villalba

Received: 3 September 2024
Revised: 20 October 2024
Accepted: 23 October 2024
Published: 29 October 2024

Copyright: © 2024 by the authors. Licensee MDPI, Basel, Switzerland. This article is an open access article distributed under the terms and conditions of the Creative Commons Attribution (CC BY) license (https://creativecommons.org/licenses/by/4.0/).

1. Introduction

For decades, reservoir engineers have been committed to seeking algorithmic models to access and predict inter-well connectivity and oil–water migration pathways, which is the key to improving oil recovery and optimizing the development scheme. Inter-well connectivity describes the efficiency of the fluid transfer pathway between injection and production wells, which is crucial for understanding reservoir dynamic behavior and formulating reasonable development strategies. Typically, high inter-well connectivity indicates the potential formation of high-permeability channels between wells. These high-permeability channels, also known as advantage seepage channels, have two-fold effects [1,2]. On the one hand, they allow fluids to pass through more easily, which

is sometimes considered beneficial during certain stages, such as the early phases of water flooding, as they can accelerate fluid flow. On the other hand, during the water flooding process, if these high-permeability channels do not effectively displace oil, they can form ineffective water circulation channels. These ineffective water circulation channels significantly reduce oil displacement efficiency, inhibit oil and gas recovery, and lead to resource wastage [3].

In recent years, with most reservoirs entering the high water cut stage, developing ineffective circulation channels between wells has become one of the main factors restricting the efficient development of oil fields [4]. By identifying and analyzing the ineffective circulation channels, the problems of low water injection efficiency, high water cuts in producers, and low recovery could be potentially addressed [5,6].

Currently, the methods used to identify ineffective circulation channels include well logging curve analysis, well testing analysis, geochemical methods, tracer testing, fuzzy comprehensive evaluation, machine learning algorithms, and capacitance-resistance model (CRM) analysis [1,7,8]. The well-logging curve method primarily determines the locations of ineffective circulation channels in reservoirs by analyzing well-logging data. However, this method is relatively simple and cannot accurately reflect reservoir changes [9]. The well-testing analysis method uses interference well testing, but it has long testing periods and high costs [10,11]. The geochemical method identifies ineffective circulation channels through chromatographic fingerprinting techniques. Although the identification results are relatively accurate, the high costs make it unsuitable for large-scale application [12]. The tracer testing method involves injecting tracers into injection wells and monitoring their output from production wells. By plotting the tracer output curves, reservoir conditions can be assessed accurately, but the method is time-consuming and expensive, making it unsuitable for large-scale deployment [13,14]. The fuzzy comprehensive evaluation method determines the evaluation indicators for inefficient circulation of oil and water wells by analyzing the influencing factors of ineffective circulation channels and their characteristics during development. While the results are objective and accurate, developing the evaluation indicators is time-consuming, and subsequent dynamic adjustments are challenging [15,16]. Machine learning algorithms such as support vector machines, random forests [17], and neural networks have also been applied to the study of ineffective circulation channels [18] (Jing et al., 2020). These methods save significant human and material resources, offer higher identification accuracy, and are suitable for widespread adoption. However, the accuracy and generalization capabilities of these models still need improvement. They face challenges in learning and adapting to unobserved tasks and have a high dependency on the training dataset [19].

The CRM analysis method for oil reservoirs has inherent advantages in quantitatively identifying ineffective circulation channels. CRM is a nonlinear, data-driven approach designed to precisely estimate the inter-well connectivities between production and injection wells under various conditions. CRM accounts for the effects of capacitance (compressibility) and resistance (transmissibility), which are represented by two key parameters: the degree of fluid storage (time constant, τ) and the degree of connectivity (weight coefficient, λ) between wells. The model utilizes injection rates as input data and production rates as output, deriving the CRM from the overall fluid mass balance within the control volume.

At present, there are many studies on the use of CRM to carry out ineffective circulation channels. Yousef et al. (2006) introduced a nonlinear data-driven CRM to accurately estimate the inter-well connectivities between production and injection wells under various conditions [20]. Sayarpour et al. (2008, 2009) presented three branches of CRM based on attributing model parameters to different control volumes: CRMT (control volume is the whole field), CRMP (each producer has a drainage volume), and CRMIP (a control volume for each injector-producer pair) [21]. Kim (2011) presented an integrated capacitance-resistance model (ICRM) that fits cumulative total production using cumulative water injection rates as inputs [22]. This approach reduces computation time by avoiding local minima issues in previous nonlinear CRMs. Salehian et al. (2018) improved the matching

performance of ICRM by employing two consecutive objective functions for monthly and cumulative liquid production matches, extending CRM applications to more realistic reservoir conditions [23]. Recently, various efforts have been made to characterize layered reservoirs using different types of CRM and their applications to conventional and smart reservoirs [24–28].

In recent years, in-depth research on CRM includes one study that explored the advantages and disadvantages of applying data-driven models of CRM in different simulation scenarios [29]; one research proposed a new method combining CRM with reservoir simulation to improve reservoir characterization and identify new development opportunities [30]; another study improved CRM model accuracy by considering variable time constant parameters during production [31]. Previous research highlighted the potential of CRM in quickly evaluating waterflood performance and discussed its application in single-well and multi-well unsaturated reservoirs [32]; Parra et al. also proposed the capacitance resistance aquifer-fractional flow model, a new approach for conventional unsaturated reservoirs in primary production [33].

Despite the progress made in the above studies, some challenges and shortcomings still remain, as summarized below:

(1) Constrained by static parameters: Although capacitance models use historical data to assess the dynamic relationships between wells, the inter-well connectivity coefficient (λ) and time-lag coefficient (τ) in the models are usually treated as fixed values. This static approach limits the models' ability to accurately capture the complex and dynamic nature of oilfield evolution, particularly when faced with continuous changes driven by field operations. Consequently, these models lack the capability to leverage advanced algorithms, such as artificial intelligence, to dynamically monitor and identify the development and extent of ineffective circulation channels, which is crucial for optimizing reservoir management.

(2) Lack of comprehensive sensitivity analysis: Different types of reservoirs have diverse geological characteristics, rock properties, and fluid properties, which introduce significant complexity in evaluating inter-well connectivity. This inherent diversity poses challenges for accurate assessments. A critical limitation of almost all existing methods is the lack of a comprehensive and unified sensitivity analysis. Specifically, there is insufficient consideration of various factors that influence inter-well connectivity. This gap in the literature necessitates a more thorough analysis.

(3) Limitations in analyzing multi-well group performance: Current studies often do not fully address the production performance of multi-well groups, specifically the formation and development of ineffective circulation channels. This oversight leads to an incomplete understanding of how these channels affect overall reservoir performance and limits the ability to optimize water injection strategies. Furthermore, the lack of in-depth analysis of the dynamics of these ineffective channels hampers efforts to enhance oil recovery effectively.

(4) Limitations of evaluation standards and field application for ineffective circulation channels: Previous research on evaluating the development of ineffective circulation channels lacks systematic and clear standards, which limits the reliability and consistency of the evaluation results. Additionally, many studies primarily rely on theoretical analysis and simulation results, lacking validation and support from actual field data, which may affect the effectiveness of the evaluation indicators in practical applications.

To address the knowledge gaps, this study proposes a state variable-based dynamic capacitance (SV-DC) model that integrates dynamic reservoir data with geological characteristics for more accurate identification of inter-well connectivity and its evolution. The model leverages injection-production data and utilizes an intelligent algorithm to solve the model efficiently, making the process simple and time-saving. A comprehensive sensitivity analysis was performed on single-well pairs and multi-well groups regarding the permeability amplitude, the width of the high permeable channel, change, and lasting period of injection pressure. In addition, the production performance of multi-well groups,

especially the development of ineffective circulation channels and their effects on reservoir development, are studied in-depth, which provides an important basis for optimizing water injection strategy and enhancing oil recovery. Finally, based on the simulation results, the evaluation index of ineffective circulation channels is proposed and applied to dozens of well groups in the entire selected oilfield, which is expected to provide a scientific basis for reservoir development.

2. Construction of the SV-DC Model

2.1. Traditional Capacitance Model

The capacitance model used for well connectivity evaluation introduced in the literature review is referred to as the traditional capacitance model (TC model) hereafter, so it can be distinguished from the new model proposed in this paper (SV-DC model). The TC model effectively captures the dynamic relationships between injectors and producers, making it a valuable tool for reservoir management. Considering a reservoir with N_i injectors and N_j producers, the total mass balance equation is [21]:

$$C_t V_{ij} \frac{d\overline{p}_{ij}}{dt} = \lambda_{ij} Q_{wi}(t) - Q_{ij}(t) \tag{1}$$

where C_t represents the compressibility; V_{ij} denotes the pore volume; Q_{ij} and $\overline{P}_{ij}$ are the flow rate and average pressure between injector i and producer j; Q_{wi} is the injection rate of injector i; λ_{ij} is a proportionality coefficient that reflects the degree of influence of injector i on producer j, known as the inter-well connectivity coefficient.

$$Q_{ij} = J_j(\overline{P_{ij}} - P_{wfj}) \tag{2}$$

where J_j is the productivity index of the production well, and P_{wfj} is the bottom-hole flowing pressure (BHP) of the production well. By taking the time derivative of Equation (2), we obtain:

$$\frac{dQ_{ij}}{dt} = J_j(\frac{d\overline{P_{ij}}}{dt} - \frac{dP_{wfj}}{dt}) \tag{3}$$

$$\frac{d\overline{P_{ij}}}{dt} = \frac{dQ_{ij}}{J_j dt} + \frac{dP_{wfj}}{dt} \tag{4}$$

Substituting Equation (4) into Equation (1), it yields:

$$C_t V_{ij}(\frac{dQ_{ij}}{J_j dt} + \frac{dP_{wfj}}{dt}) = \lambda_{ij} Q_{wi}(t) - Q_{ij}(t) \tag{5}$$

Equation (6) links the pore volume (connectivity volume) V_{ij} and τ_{ij} [20]:

$$\tau_{ij} = \frac{C_t V_{ij}}{J_j} \tag{6}$$

where τ_{ij} is the first order system's time constant and indicates how quickly the reservoir responds to changes in injection rates. Although calculated as a static parameter, τ_{ij} varies dynamically in real reservoir conditions.

Combining Equations (5) and (6) yields:

$$\tau_{ij} \frac{dQ_{ij}}{dt} = \lambda_{ij} Q_{wi}(t) - Q_{ij}(t) - \tau_{ij} J_j \frac{dP_{wfj}}{dt} \tag{7}$$

After reviewing the method used by previous researchers [34], it has been observed that as producer bottom pressure fluctuates much less than the production rate, the influ-

ence of the pressure term can be regarded as a secondary factor. Consequently, Equation (7) can be simplified into the following:

$$\tau_{ij}\frac{dQ_{ij}}{dt} = \lambda_{ij}Q_{wi}(t) - Q_{ij}(t) \tag{8}$$

Solving the differential equation for Equation (8) yields the following:

$$Q_{ij}(t) = Q_{ij}(t_0)e^{-\frac{t-t_0}{\tau_{ij}}} + \int_{t_0}^{t}\frac{\lambda_{ij}}{\tau_{ij}}Q_{wi}(\zeta)e^{-\frac{t-\zeta}{\tau_{ij}}}d\zeta \tag{9}$$

Taking into account that the total production rate $Q_j(t)$ is the combined contributions from all injectors N_i to the producer j, the total production rate $Q_j(t)$ can be expanded as:

$$Q_j(t) = \sum_{i=1}^{N_i}Q_{ij}(t) = \sum_{i=1}^{N_i}Q_{ij}(t_0)e^{\frac{-(t-t_0)}{\tau_{ij}}} + \sum_{i=1}^{N_i}\lambda_{ij}\frac{e^{-\frac{t}{\tau_{ij}}}}{\tau_{ij}}\int_{t_0}^{t}e^{\frac{\zeta}{\tau_{ij}}}Q_{wi}(\zeta)d\zeta \tag{10}$$

Then, Equation (10) can be discretized with monthly intervals. The first term on the right of the equals sign is a time-dependent variable correlated with the initial production and decays exponentially over time as follows:

$$\beta_j(n) = \textstyle\sum_{i=1}^{N_i}Q_{ij}(0)e^{-\frac{n}{\tau_{ij}}} \tag{11}$$

Thus, the discretized form of Equation (10) is given by

$$Q_j(n) = \beta_j(n) + \sum_{i=1}^{N_i}\lambda_{ij}\sum_{m=n_0}^{m=n}\frac{1}{\tau_{ij}}e^{\frac{(m-n)}{\tau_{ij}}}Q_{wi}(m) \tag{12}$$

where $Q_j(n)$ represents the producer's total production j in time step n, n_0 is the initial time, m and n are the time step indexes.

The above derivation process is well documented elsewhere [34,35] and lays the theoretical foundation of the TC model. The time-lag coefficient τ_{ij} is a dimensionless time constant representing the transfer time between wells. The TC model shows that the cumulative production of a producer is determined by the combined effect of its initial cumulative production and the historical injection activity.

2.2. State Variable-Dynamic Capacitance Model

The construction of the SV-DC model in this study begins with the extraction of state variables using the EKF (extended Kalman filtering) algorithm, as established in previous works [36], where state variable models were based on pressure impulse responses and solved using the EKF algorithm.

In the SV-DC model, three state variables that appear in Equation (12) β_j, λ_{ij}, and τ_{ij} are defined and extracted as state variables since they are the key parameters controlling the dynamic response characteristics of a reservoir. These variables are integral to the model and can be effectively estimated using the EKF algorithm. Consequently, Equation (12) can be transformed by a 3×1 state vector $x_j(m)$:

$$\begin{aligned} x_i(m) &= \left[\ x(m),\quad x_1(m),\quad x_2(m)\ \right]' \\ &= \left[\ \beta_j(m),\quad \lambda_{ij}(m),\quad \tau_{ij}(m)\ \right]' \end{aligned} \tag{13}$$

Using standard techniques [37], the state variables are

$$\begin{cases} x_i(n) = \begin{bmatrix} x(m) \\ x_{i1}(m) \\ x_{i2}(m) \end{bmatrix} + n_{xi}(m) \\ p_i^c(n) = \left[1 \sum_{m=n_0}^{n} \frac{1}{\tau} e^{\frac{(m-n)}{\tau_{ij}}} Q_{wi}(m) \sum_{i=1}^{N_i} \lambda_{ij} \sum_{m=n_0}^{n} \left(-\frac{1}{\tau_{ij}^2} e^{\frac{(m-n)}{\tau_{ij}}} Q_{wi}(m) - \frac{(m-n)}{\tau_{ij}^2} e^{\frac{(m-n)}{\tau_{ij}}} Q_{wi}(m) \right) \right] x_i(n) \end{cases} \tag{14}$$

Aggregating the state vectors of all N injectors, a complete $1 + 2N$ state vector is obtained,

$$x_i(m) = \left[\beta_j(m), \quad \lambda_{1j}(m), \quad \tau_{1j}(m), \quad \lambda_{2j}(m), \quad \tau_{2j}(m), \quad \cdots, \quad \lambda_{Nj}(m), \quad \tau_{Nj}(m) \right]' \tag{15}$$

The state variables for the entire producer-centric system are given in Equation (16):

$$\begin{cases} x(n) = \begin{Bmatrix} x_1(m) \\ x_{11}(m) \\ x_{12}(m) \\ x_{21}(m) \\ x_{22}(m) \\ \vdots \\ x_{N1}(m) \\ x_{N2}(m) \end{Bmatrix} + n_x(m) \\ p(n) \quad = p_1^c(n) + p_2^c(n) \cdots + p_N^c(n) + n_p(n) \\ \qquad = Hx(n) + n_p(n) \end{cases} \tag{16}$$

To find the measurement matrix H in Equation (16), one needs to linearize the measurement equation Equation (12) using Taylor series expansion to obtain H. Let Equation (12) be h, it yields the following:

$$\varepsilon = \frac{\partial h}{\partial x} \tag{17}$$

$$\varepsilon = \left[1 \sum_{m=n_0}^{n} \frac{1}{\tau} e^{\frac{(m-n)}{\tau_{ij}}} Q_{wi}(m) \sum_{i=1}^{N_i} \lambda_{ij} \sum_{m=n_0}^{n} \left(-\frac{1}{\tau_{ij}^2} e^{\frac{(m-n)}{\tau_{ij}}} Q_{wi}(m) - \frac{(m-n)}{\tau_{ij}^2} e^{\frac{(m-n)}{\tau_{ij}}} Q_{wi}(m) \right) \right] \tag{18}$$

$$\varepsilon' = \left[\sum_{m=n_0}^{n} \frac{1}{\tau} e^{\frac{(m-n)}{\tau_{ij}}} Q_{wi}(m) \sum_{i=1}^{N_i} \lambda_{ij} \sum_{m=n_0}^{n} \left(-\frac{1}{\tau_{ij}^2} e^{\frac{(m-n)}{\tau_{ij}}} Q_{wi}(m) - \frac{(m-n)}{\tau_{ij}^2} e^{\frac{(m-n)}{\tau_{ij}}} Q_{wi}(m) \right) \right] \tag{19}$$

$$H = \left[1 \; \varepsilon_1' \; \varepsilon_2' \cdots \varepsilon_N' \right] \tag{20}$$

The complete state variables for all injector subsystems are given in Equation (16), where $p(n)$ is the measured production rate, and $n_x(m)$ and $n_p(n)$ are additive zero-mean white noises for the state and measurement equations. The treatment of the state variables in developing the SV-DC model is expounded through the streamlined logical sequence provided in Equation (13) to Equation (20). For the computation outlined in Equation (13) to Equation (20), applying the EKF algorithm is essential, as it shows proficiency in managing nonlinearity and providing dynamic state estimation. Integrating the EKF algorithm with the state variables model enables us to dynamically characterize the well connectivity and time-lag coefficient, offering a more accurate and temporally responsive representation of reservoir dynamics.

2.3. Procedures of the EKF Algorithm

The Kalman Filter method is a mathematical optimization technique originally developed for signal control. It has since been adapted to various fields, including nonlinear systems. The nonlinear EKF algorithm, as an extension of the Kalman Filter, contains four stages: system prediction, establishing measurement equations, generating optimal estimates, and updating the error covariance. The workflow presented in Figure 1 is the core idea of evaluating inter-well connectivity using the EKF algorithm [36,38,39].

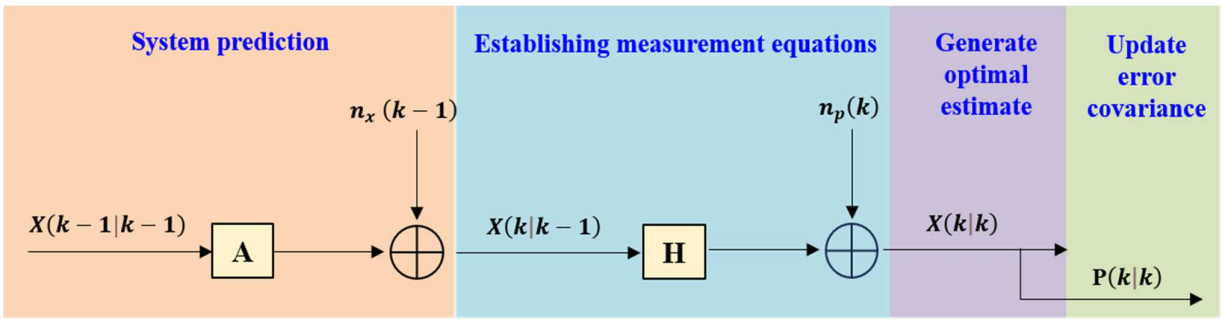


Figure 1. Flowchart of calculating inter-well connectivity using the EKF algorithm.

(1) System prediction

To further highlight the advantages of autoregressive at each step provided in the EKF algorithm, m in Equation (12) is represented by $k-1$ and n is represented by k.

$$X(k|k-1) = FX(k-1|k-1) + n_x(k-1) \tag{21}$$

$$P(k|k-1) = FP(k-1|k-1)F^T + Q \tag{22}$$

where X is a representation of the set of state variables in Equation (15), and $X(k|k-1)$ denotes the prediction of the current step's state variables using the state variables from the last step. F is the state transition matrix of the system. $n_x(k-1)$ is the system noise. Overall, Equation (21) uses the optimal estimate $X(k-1|k-1)$ from the last step, the system matrix F, and the noise n_x to predict the state variables at the current step.

Similarly, Equation (22) uses the optimal estimate $P(k|k-1)$ from the last step (P is the error covariance of the optimal estimate), the system matrix F, and Q (Q is the covariance matrix of noise n_x) to predict the error covariance of the optimal estimate at the current step $P(k|k-1)$.

The state transition matrix F is a $3N \times 3N$ Jacobian matrix, the explicit form of which is given below for the nonlinear state equation in Equations (23) and (24):

$$F_x = \begin{bmatrix} A_1 & \underline{0} & \cdots & \underline{0} \\ \underline{0} & A_2 & \ddots & \vdots \\ \vdots & \ddots & \ddots & \underline{0} \\ \underline{0} & \cdots & \underline{0} & A_N \end{bmatrix} \tag{23}$$

$$A_i = \begin{bmatrix} 1 & 0 & 0 \\ 0 & 1 & 0 \\ 0 & 0 & 1 \end{bmatrix} \tag{24}$$

(2) Establishment of the measurement equation

The measurement equation describes the relationship between the state variables and the actual observations. For the system state variable $X(k)$, one can observe the variable associated with $Z(k)$, as expressed as:

$$Z(k) = HX(k) + n_p(k) \tag{25}$$

where Z is the observed value of the variables. H is the observation matrix, and n_p is the measurement noise.

(3) Optimal estimation generation

The generation of optimal estimation mainly consists of calculating the Kalman gain Equation (26) and establishing the optimal estimate equation Equation (27).

$$K_g(k) = \frac{P(k|k-1)H^T}{HP(k|k-1)H^T + R} \tag{26}$$

$$X(k|k) = X(k|k-1) + K_g(k)[Z(k) - HX(k|k-1)] \tag{27}$$

The core idea of the EKF algorithm is to combine model predictions with actual measurements to obtain an optimal state estimate by searching for the minimum mean square of the estimation error. This process requires finding a gain K_g that minimizes the mean square of the estimation error, as expressed in Equation (26), after a series of mathematical derivations.

Equation (27) represents a correction based on the difference (i.e., the residual) between the predicted state variable X and the actual measurement Z. This perspective K_g determines the extent to which the predicted state variables are corrected based on the measurement residuals. It should be noted that the $X(k|k-1)$ in the a priori estimation equation differs from the $X(k)$ in the measurement equation. $X(k|k-1)$ is obtained from the prediction of the system state at the step $(k-1)$; whereas, $X(k)$ is the measurement at the step k, which is independent of the values of the measurements at the last step.

(4) Error covariance update

The final process of updating the error covariance can be performed using Equation (28),

$$P(k|k) = \left[1 - K_g(k)H\right]P(k|k-1) \tag{28}$$

As the last stage of the EKF algorithm, it ensures that the estimate is optimum and matches the real uncertainty.

The main idea of the extended Kalman filter (EKF) is to linearize the nonlinear system using a first-order Taylor expansion to approximate the state and observation equations, enabling the Kalman filter to be used for nonlinear systems. The entire process consists of four stages. First is the system prediction stage, where the dynamic model is used to predict the state at the next time step while also accounting for process noise and uncertainty. Next is the establishment of measurement equations, which combines the predicted state with the measurement model to reflect the actual observed values of the system while considering the impact of measurement noise. In the generation of the optimal estimate stage, the predicted values are combined with the observed values to adjust the state estimate, making it more accurate. This is the key step of the filtering process, as it integrates observational information with the predicted results. Finally, there is the update of the error covariance, which reflects the changes in uncertainty in the current estimate, ensuring that the estimation remains optimal and matches the actual uncertainty. The advantage of the EKF is that even for nonlinear systems, it can achieve a good estimation effect through linear approximations using the Jacobian matrix, thus maintaining high reliability and applicability when dealing with complex nonlinear problems.

3. Construction of Numerical Model

3.1. Project Background

Qinhuangdao Oilfield 32-6, located in Bohai Bay, is a large, thick oil field with complex fluvial features, whose main reservoirs are the lower part of the Neoproterozoic Minghuazhen Formation and the upper part of the Guantao Formation. The oilfield is characterized by high porosity (32% on average) and high permeability (2–8474 mD) as well as medium to high crude oil viscosity (22–260 mPa·s).

The distribution of oil layers and well location in the Qinhuangdao Oilfield 32-6 is shown in Figure 2. Wells in Qinhuangdao Oilfield 32-6 are being produced with fixed BHP adopting stimulation measures, such as leakage plugging, which has greatly improved the output. Brine saturated with the active agent was injected into the formation to displace oil, and the injection pressure, according to the monitoring results, fluctuated significantly. Currently, the field faces problems of increased dynamic inhomogeneity and ineffective water circulation caused by long-term development, especially after the main sand body enters the high water content stage.

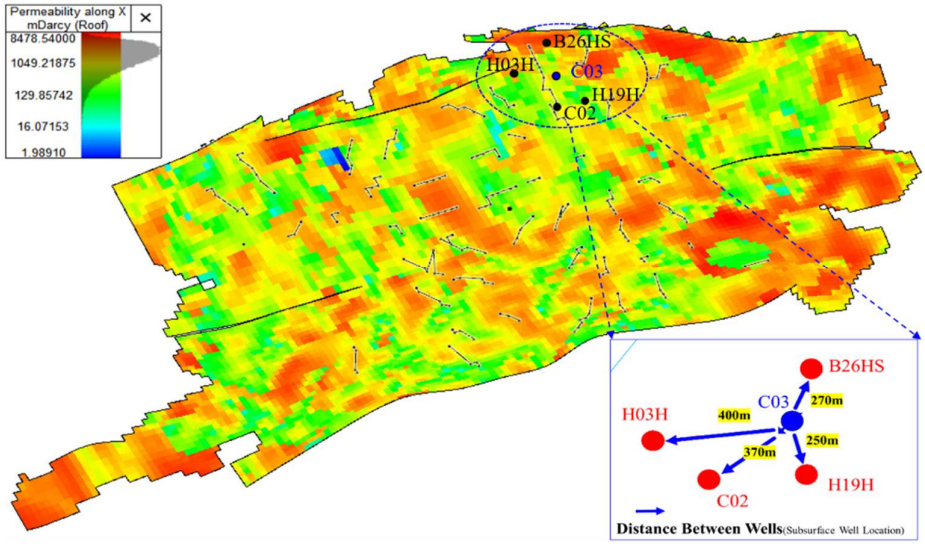


Figure 2. Geological overview of the Nm13 sand body in southern Qinhuangdao 32-6 oilfield. The black lines in the larger image indicate potential faults detected, and the blue dot in the zoomed image represent the central one injector, and the four red dots represent the four producers peripherally.

3.2. Model Construction

SV-DC model analysis requires comprehensive and continuous data, which can be accessible by either numerical simulation or field monitoring. Compared with the field monitoring data that are often incomplete and susceptible to events such as well leakage, equipment failure, and shut-in maintenance, numerical simulation can ensure the integrity and continuity of data. When constructing the SV-DC model, the EKF algorithm requires the data to be continuous, complete, and uninterrupted. The numerical data meet all these strict requirements. With this in mind, this paper chose data based on numerical simulation rather than directly using field data to reveal the influence law of inter-well connectivity and perform the sensitivity analyses.

This study chooses the widely used reservoir simulator tNavigator (Version 23.3) to simulate oilfield production [40]. The tNavigator is a new efficient reservoir numerical simulation system that combines static (geological) and dynamic (reservoir) models comprehensively. The tNavigator is the first industry-leading product that dynamically integrates a fully 3D interactive user interface with a record-breaking CPU+GPU co-parallel computing engine.

A 3D reservoir model with 305 m × 305 m × 5 m (length × width × height) was developed according to the geology data (Figure 3a). A single oil formation was considered with a thickness of 5 m according to the average oil layer thickness. A typical five-spot well pattern was adopted. According to the model symmetry, a one-quarter model was considered with the production well and injection well arranged at the corners of the rectangle model domain (Figure 3b). A high-permeable channel was simulated along the model diagonal with varied absolute permeabilities and channel widths.

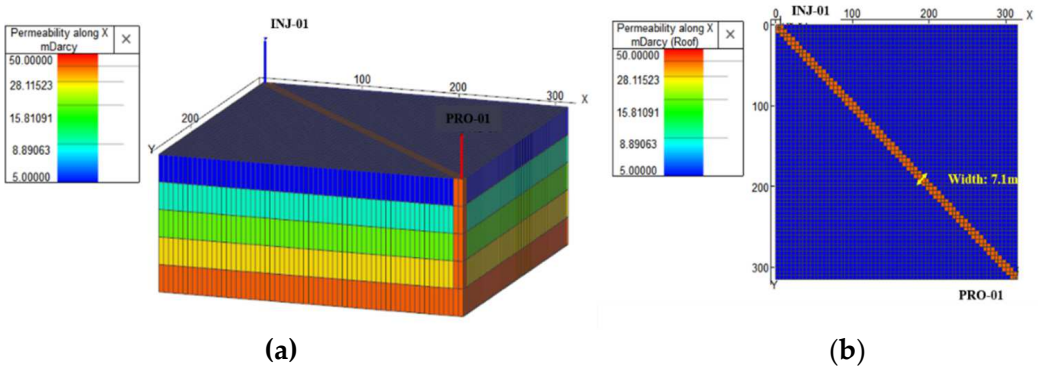


Figure 3. Three-dimensional reservoir model (**a**) and high-permeability channel between injector and producer (**b**).

The production well BHP was set at 600 bar throughout the run (Table 1). Initially, the injection well had a BHP of 750 bar, which was subsequently adjusted to 780 bar, 800 bar, and 760 bar at different stages. These adjustments occurred as distinct rectangular impulse signals. The adjustments were scheduled for January 2024, January 2027, and January 2031, with each adjustment period lasting six months.

Table 1. Model setup for injection and production wells.

Production Well BHP (Bar)	Reservoir Average Pressure (Bar)	Injection Pressure Regulation (Bar)	Each Pressure Regulation Duration (Month)	Distance Between Injector and Producer (m)
600	750	780, 800, 760	6	424.3

The petrophysical parameters of the ideal reservoir model are listed in Table 2. The reservoir porosity and matrix permeability of the model were assigned as 2% and 10 mD, respectively. Water density was assumed to be 1000 kg/m^3, and the oil density was estimated to be the average oil density (867 kg/m^3) of most oil fields in China.

Table 2. Petrophysical parameters used in the ideal model.

Parameters	Value	Unit
Depth	6000	m
Porosity	2	%
Initial water saturation	0.2	/
Matrix permeability	5	mD
High-permeability channel permeability	30/60/90/120	mD
Oil density (at surface conditions)	867	kg/m^3
Water density (at surface conditions)	1000	kg/m^3
BHP of productor	600	bar
BHP of injector	750	bar

4. Production Performance of Single Well Pair

The numerical simulation is first carried out on a single well pair. The producer is produced under a constant BHP, and the injection pressure of the injector adopts a unit step signal to represent the pressure impulses. The SV-DC model is used to calculate the inter-well connectivity coefficient and time-lag coefficient, and the changes in these coefficients under different permeability channels are studied to reveal the influence of geological heterogeneity on reservoir production.

4.1. Fluid Migration

In Figure 4, the liquid production rate consists of oil and water production rates. Significant water injection and liquid production rate increases were observed at certain moments (January 2024, January 2027, and January 2031). Especially in 2027, the injection volume soars to over 4 m^3/day. This phenomenon is closely related to the production system of the assumed single-well pair system. In 2024, 2027, and 2031, the BHP of injector increases from 750 bar to 780 bar, 800 bar, and 760 bar, respectively. Therefore, the increase in pressure directly promotes the increase in injection volume and liquid production, and the maximum production pressure differential corresponds to the maximum liquid production.

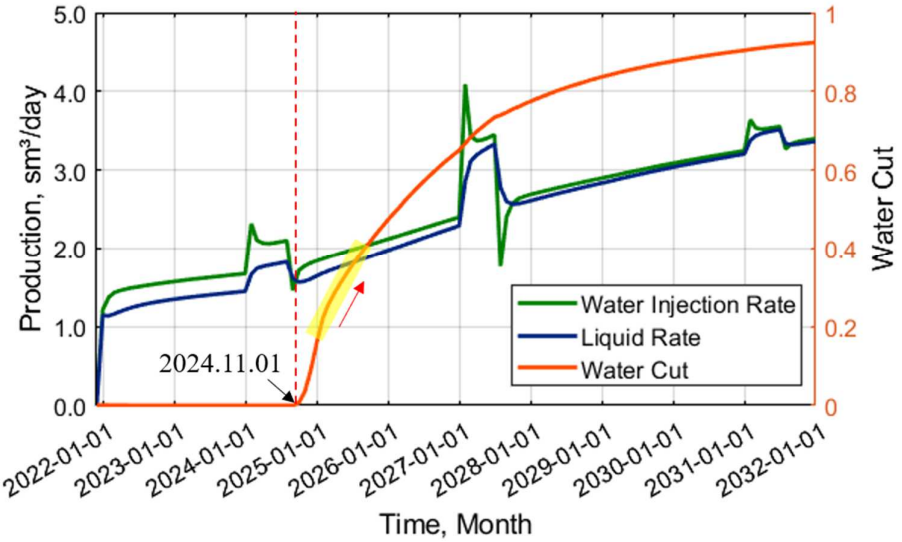


Figure 4. Variation in water injection rate, liquid production rate, and producer water cut affected by artificially applied pressure impulses.

Further examination of the relationship between the water injection rate and liquid production rate suggests that the water injection rate increases simultaneously with the increase in injection pressure. In contrast, the production rate increases slowly after the pressure impulses are applied and decreases slowly after the removal of pressure impulses. In a complex reservoir system, the water injection from the injector can be treated as the input signal while the production is deemed the output signal. This delayed response in fluid production observed in Figure 4 is essentially a reflection of the attenuation of the reservoir system to pressure signals. In general, for a fixed well spacing, the presence of low permeability zones, faults, and the high viscosity of reservoir fluids will all exert a large dissipative effect on the injection signals, which leads to a delay in the fluid production.

In Figure 4, the water cut profile is also plotted against the water injection and liquid production curves. Water cut refers to the mass percentage of water in a producing well, thus showing an increasing trend with production. The initial water cut is zero until 1 November 2024, followed by a rapid increase to 0.7 within one year, and then the water cut slowly increases to 0.92 in the following simulation. The sudden response of the water cut profile facilitates locating the water breakthrough time of the producer.

Figure 5 illustrates the variation in oil saturation in the reservoir at three consecutive time points, combined with the water cut, which helps ascertain the time of water breakthrough. The modeled water breakthrough happens on November 2024, when a connected water flow pathway is formed in the reservoir, allowing water to flow more efficiently to the producer along the model diagonal. This observation is consistent with the time-dependent water cut profile in Figure 4.

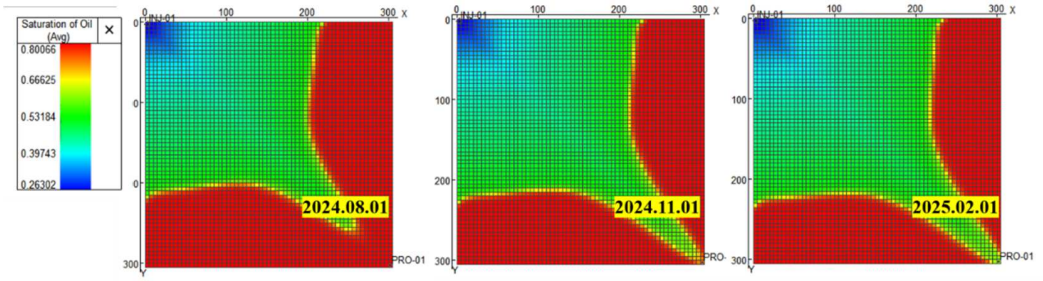


Figure 5. Variation in oil saturation with time (the predicted water breakthrough time is about 1 November 2024, as highlighted by the middle picture).

In Figure 5, the water cone has not yet reached the producer on 1 August 2024; on 1 November 2024, the water cone has just contacted the producer; and on 1 February 2024, the water cone has been rippling through the producer for some time. The simulation also suggests that for the oil beyond the water cone, it is almost impossible to be displaced without well pattern thickening or well groups conversion. The formation of advantageous water flooding channels is one of the main factors affecting the efficiency of oil recovery [41,42].

4.2. Connectivity Analysis of Single Well Pair

Based on the simulation's fluid production and injection data, the SV-DC model can be used to calculate the inter-well connectivity and time-lag coefficients and further explore inter-well fluid migration characteristics. Figure 6 shows the results of the time-dependent inter-well connectivity coefficient and time-lag coefficient.

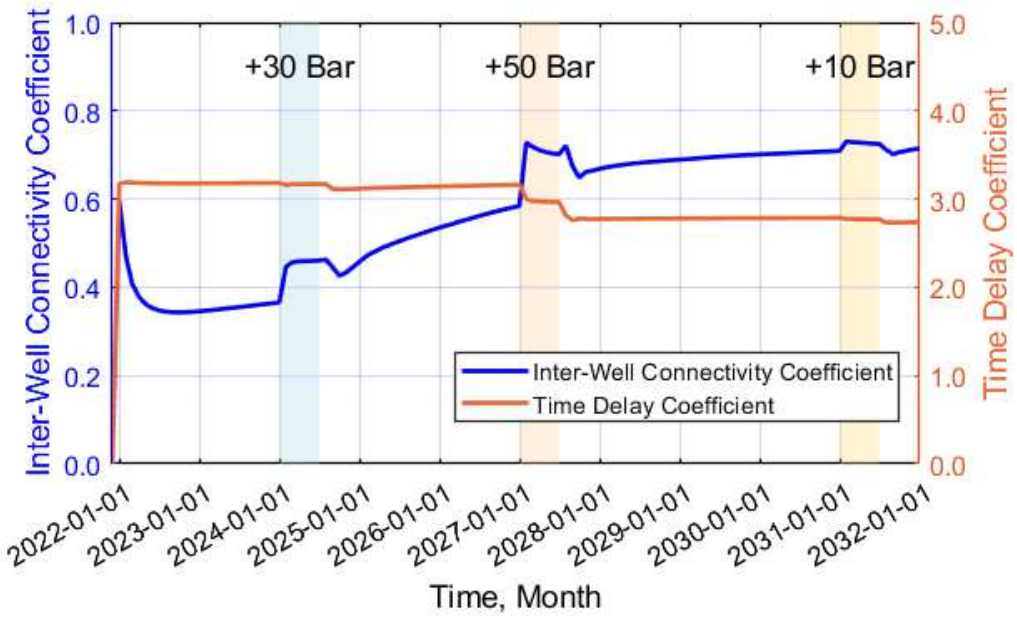


Figure 6. Dynamic changes in inter-well connectivity coefficient and time-lag coefficient.

In Figure 6, the inter-well connectivity coefficient shows a continued upward trend overall. This indicates increased connectivity between the injector and producer over time. During the increase in injection pressure differential, the connectivity coefficient peaks, and the increment is proportional to the scale of the pressure differential.

The time-lag coefficient remains stable most of the time, indicating that the production reaction to injection was relatively constant. However, subjected to the increasing pressure differential, the time-lag coefficient between wells decreases, and the descend range is inversely proportional to the pressure differential. This inverse relationship may indicate that a higher pressure differential causes the fluid to move to the producer more quickly, thus shortening the fluid migration time, yielding a reduced time-lag coefficient.

In summary, the variations in the inter-well connectivity coefficient and time-lag coefficient during the injection pressure fluctuation period account for the direct effect of injection pressure on fluid migration. The increase in connectivity coefficient and the decrease in time-lag coefficient reflect the change in reservoir fluid dynamics in the case of increasing injection pressure, in which time the ineffective circulation channels may be formed.

4.3. Sensitivity Analysis of Inter-Well Connectivity

In the above analysis, it has been found that applying pressure stimulation leads to a noticeable response in inter-well connectivity. This section further explores the effect of the pressure impulse duration and amplitude on inter-well connectivity. In addition, the effect of high permeable channels is also examined. Due to the complex geological conditions of the reservoir, a high permeable channel plays a crucial role in determining the breakthrough time of the water cone and the development of ineffective circulation channels. The detailed setting and parameter ranges of the sensitivity studies are shown in Table 3 below, including the permeability of the permeable channel (scenario 1), the width of the permeable channel (scenario 2), injection pressure duration (scenario 3), and injection pressure differential (scenario 4).

Table 3. Basic parameters for sensitivity analysis of inter-well connectivity.

Scenario	Injection Pressure (Bar)	Pressure Change Duration (Month)	Producer BHP (Bar)	Channel Width (m)	Channel Permeability (mD)
1	780, 800, 760	6	600	7.1	30, 60, 90, 120
2	780, 800, 760	6	600	7.1, 14.1, 21.1, 28.3	30
3	780, 800, 760	2, 6, 12	600	7.1	30
4	780, 800, 760	6	600	7.1	30

4.3.1. Permeability of Permeable Channels

The high-permeability channel is oriented along the diagonal connecting the injector and producer and has an initial width of 14.1 m (the grid side is 5 m long). The permeability of the matrix is 5 mD, and the permeability of the permeable channel is chosen to be four separate values with identical intervals (30 mD, 60 mD, 90 mD, and 120 mD). Figure 7 shows a significant positive correlation between the channel permeability and inter-well connectivity coefficient. The reason is that high permeability improves the ability of the fluid to migrate within the reservoir, making the production well more sensitive to the response of the applied pressure impulses.

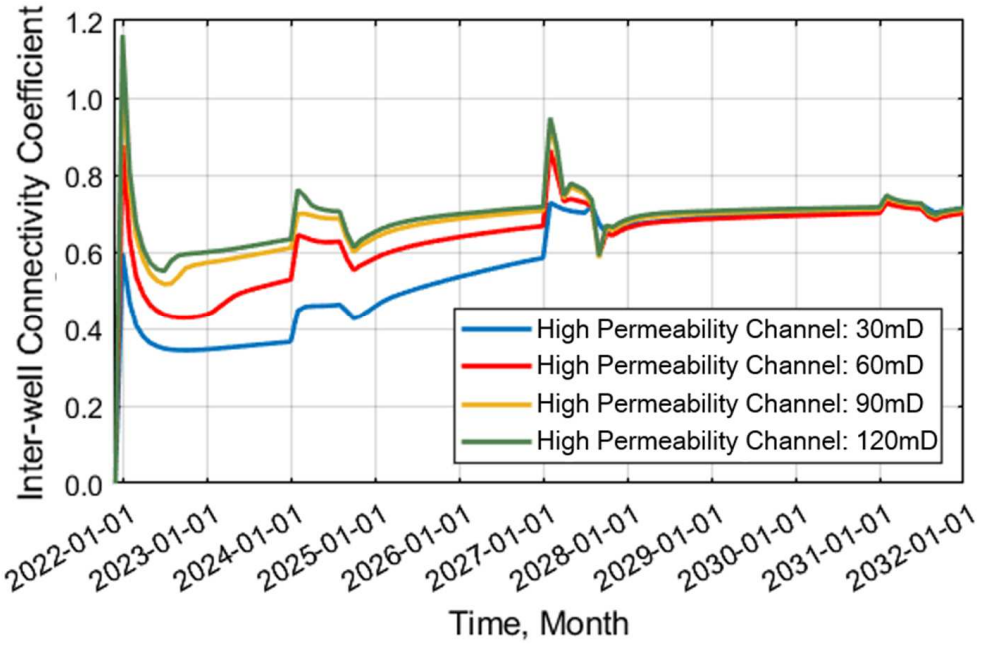


Figure 7. Dynamic changes in inter-well connectivity coefficients over time for permeable channels.

Interestingly, the inter-well connectivity during the pressure stimulation stages is significantly higher than that of the non-pressure stimulation stages. When the channel permeability reaches 90 mD and 120 mD, the effect of increasing permeability on the inter-well connectivity becomes insignificant.

In the later stage of production, roughly corresponding to 1 June 2027, the connectivity coefficients under different permeability channels tend to be stabilized within a certain range (0.65–0.75) since the water occupies the pore space under high water content and the mobility of water in all permeable channels is transferred from two-phase oil–water flow to single-phase water flow. Therefore, the connectivity differences caused by varied permeability channels may be weakened.

Figure 8 shows the dynamic change in the dimensionless time-lag coefficient τ, a key indicator of the time required for fluid to flow from the injector to the producer. According to the calculation results, it is observed that the relationship between the τ value of the four producers is $\tau_{30} > \tau_{60} > \tau_{90} > \tau_{120}$ that is, the τ value is inversely proportional to the permeability. This indicates that fluid migration rates are accelerated within a higher permeability channel, resulting in a faster fluid flow to the producer. This finding is consistent with observations at the time of the water breakthrough. Since the fluid flow rate is directly related to the formation permeability, fluid mobility is enhanced in the advantage channel with high permeability, giving it a lower time-lag coefficient.

As can be seen from Figure 9, there is an obvious negative correlation between permeability and water breakthrough time. A producer connected to the center injector at a permeability of 30 mD has a water breakthrough time of 24 months. For producers with 60 mD permeability channels, the water is encountered after 12 months of production. However, the water breakthrough times for producers with 90 mD and 120 mD permeability are 6 months and 5 months, respectively.

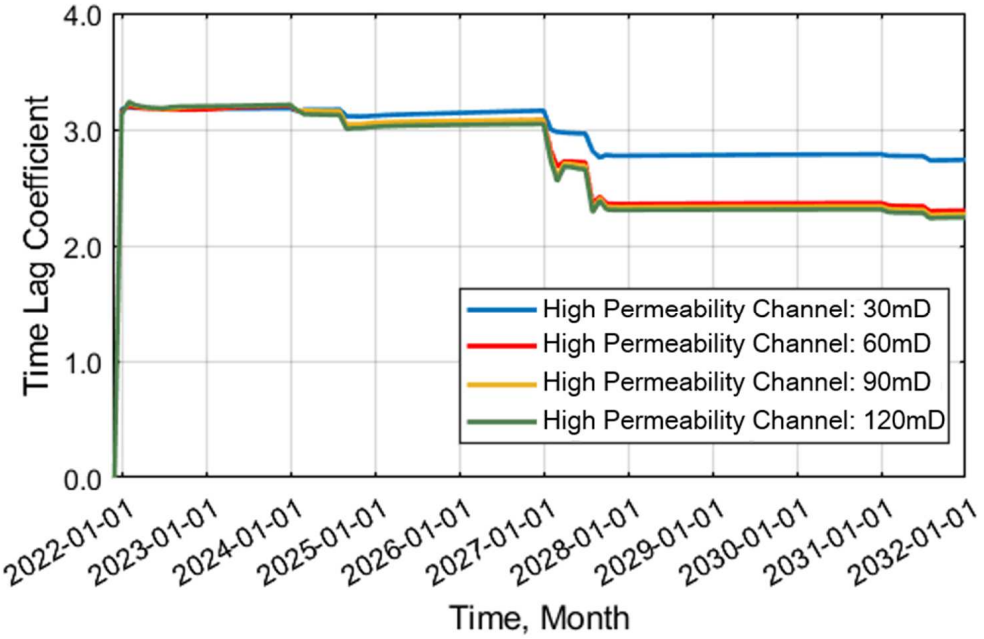


Figure 8. Dynamic changes in time-lag coefficients with time under different permeable channels.

This indicates that injected fluid can move more rapidly through the higher permeability channels, resulting in an earlier appearance of injected water in the producer. This phenomenon is twofold: higher water injection efficiency is its advantage, but it is also accompanied by the risk of water-driven fingering (increasing the cost of water plugging), lowering the water sweep efficiency, and jeopardizing the life cycle of the oil wells.

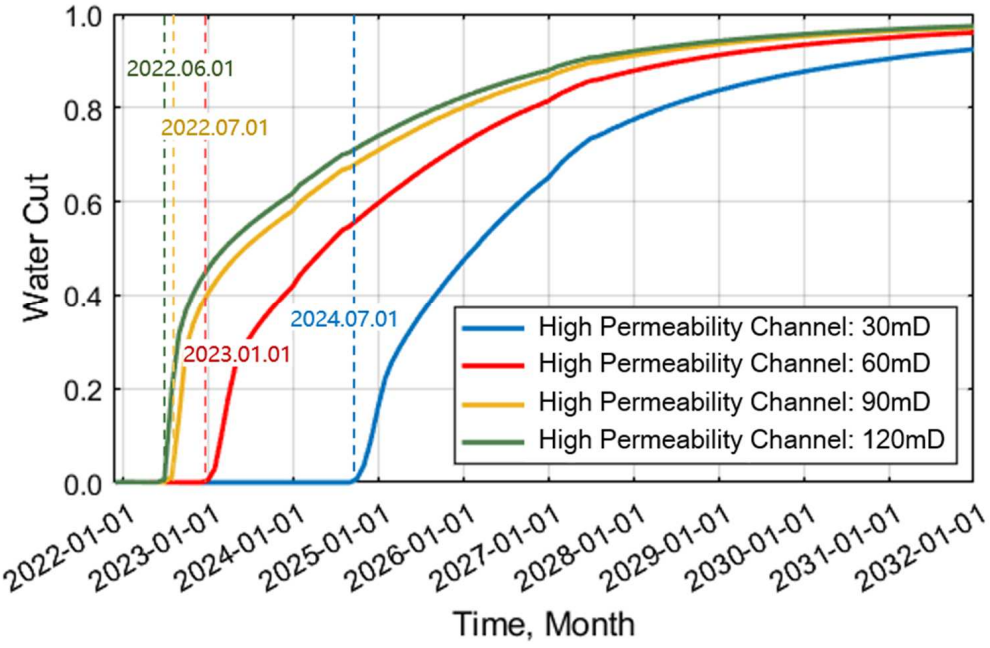


Figure 9. Water cut profiles observed under different reservoir permeability channels.

4.3.2. Width of Permeable Channels

Figure 10 shows the variations in the inter-well connectivity coefficient with time under four different channel widths (7.1 m, 14.1 m, 21.1 m, 28.3 m). The connectivity coefficient experiences a corresponding increasing trend with the increased channel width. The reason is that a wider channel means a larger effective conductive area, which enhances the fluid flow capacity and thus improves fluid production, increasing inter-well connectivity. In particular, channel width is more significant in the medium water cut stage, during which the oil and water flow pathways may be altered frequently and become complex due to the applied pressure impulses.

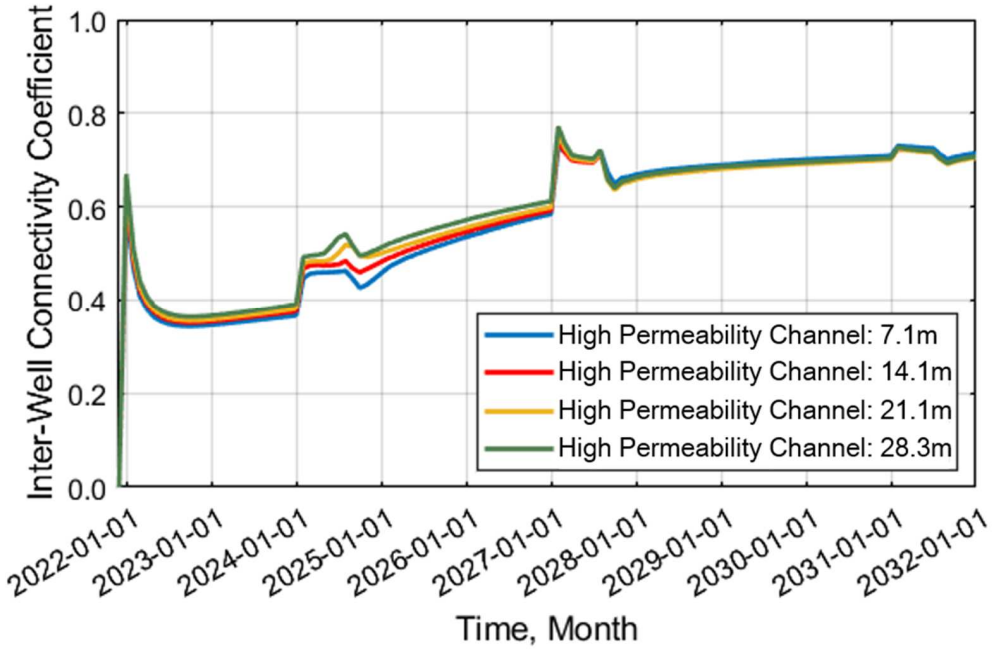


Figure 10. Inter-well connectivity coefficients for different high permeable channel widths.

Nevertheless, with the passage of time, the connectivity coefficients of each width channel tend to be stable. This convergence may mean that in the later production stages, as the water phase dominates, the difference in the influence of different widths of high permeable channels on inter-well connectivity is reduced. Therefore, the width of the high permeable channel may affect the initial flow in the reservoir, and the effect decreases gradually with the increase in water saturation.

The time-lag coefficients for all channels with different widths show a steady downward trend subjected to the pressure impulses, implying an improvement in fluid transfer efficiency, as shown in Figure 11. With the increase in the width of permeable channels, the time-lag coefficient decreases obviously. It reaches the minimum for a wider permeability channel, indicating that the higher the width of the permeable channel, the faster the fluid dynamic response. Previous studies also confirmed that a wider permeability band could more effectively promote the rapid flow of oil and water and shape the two phases' contact surface, thus accelerating the speed of fluid dynamic response [43,44].

From the long-term run, the time-lag coefficients at different widths of permeable channels tend to be a relatively close-set, which may mean that with the continuous development of the reservoir, the overall fluid transfer efficiency for different permeable channels tends to be consistent.

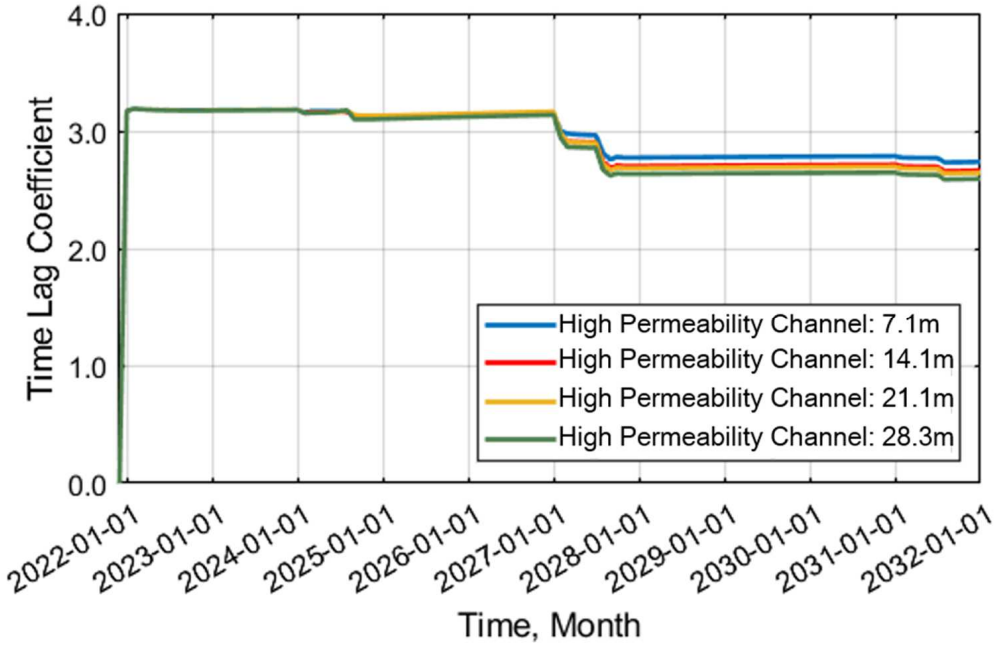


Figure 11. Variations in time-lag coefficients under different widths of permeable channels.

4.3.3. Duration of Pressure Impulses

Figure 12 shows the variation in inter-well connectivity coefficient for different pressure impulse durations, which are 3 months, 6 months, 9 months, and 12 months, respectively. It is found that after the first pressure impulse is applied, there is a significant increase in the connectivity coefficient. It is most likely that the applied pressure impulses stimulate fluid migration, facilitating a dominant water flow channel. Notably, the second pressure impulse with the highest amplitude (+20 bar) corresponded to a more significant rise in the connectivity coefficient.

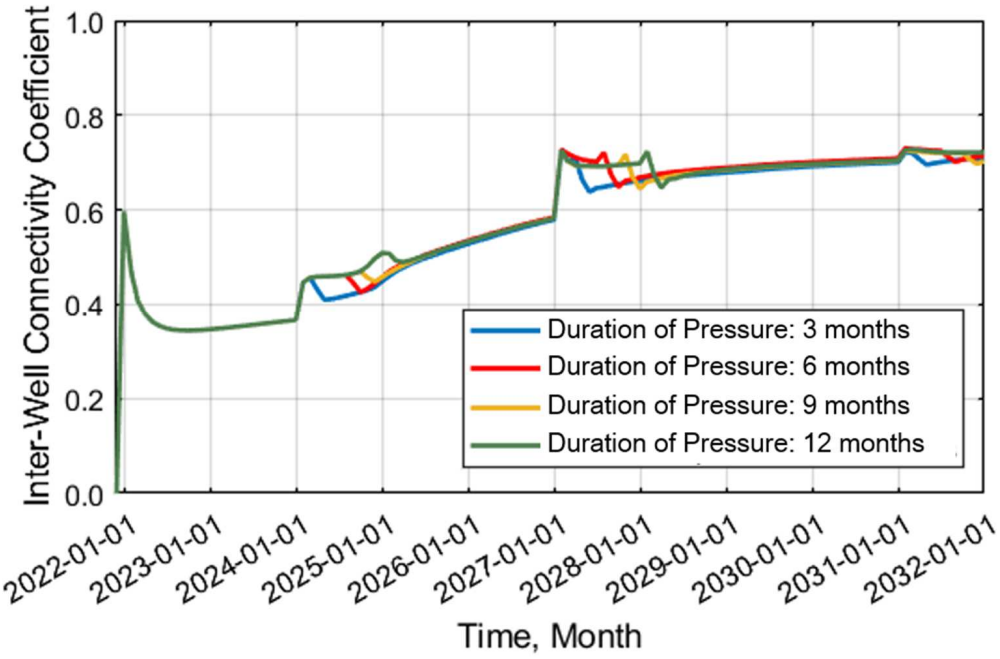


Figure 12. Inter-well connectivity coefficients for different pressure impulse durations.

With the increase in the duration of pressure impulses, the inter-well connectivity coefficient increases, which may be because the longer pressure differential provides more possibilities for oil and water migration and exchange, which is conducive to enhance the inter-well connectivity.

However, once the applied injection pressure differential is over, the connectivity coefficients for each pressure differential are consistent, indicating a similar flow pattern and equilibrium state. From a long-term perspective, inter-well connectivity eventually shows a consistent trend regardless of how long the injection pressure differential lasts.

The time-lag coefficient decreases steadily under different durations of pressure impulses, indicating an improved fluid transfer efficiency in the reservoir, and the impact of water injection can be felt more quickly in the producers. At the same time, it is observed in Figure 13 that the time when the time-lag coefficient begins to decline is related to the time when the injection pressure differential plays a role. For the pressure differential duration of 3 months, the decline of the time-lag coefficient starts earlier, but at 12 months, the decline of the time-lag coefficient commences later. This shows a swift self-adaptation and recovery of the fluid transfer system when the reservoir experiences a short-term pressure impulse. In contrast, long-term pressure differential causes the fluid flow system to respond steadily after adjustment. This trend may be related to reservoir fluid dynamics and the establishment of ineffective circulation channels. Short-term pressure differential may cause rapid fluid movement and redistribution in the reservoir, while long-term pressure differential may cause far-reaching adjustments in the fluid flow path. Once the change in injection pressure differential ends, the time-lag coefficients of each period eventually converge, indicating that the reservoir has reached a new dynamic equilibrium state. On the whole, the change in time-lag coefficients under different pressure differential durations reflects the adaptability and recovery of the reservoir to operation schedule changes. This insight is valuable for developing and adjusting oil field development strategies, especially when designing water injection schemes and predicting long-term field performance.

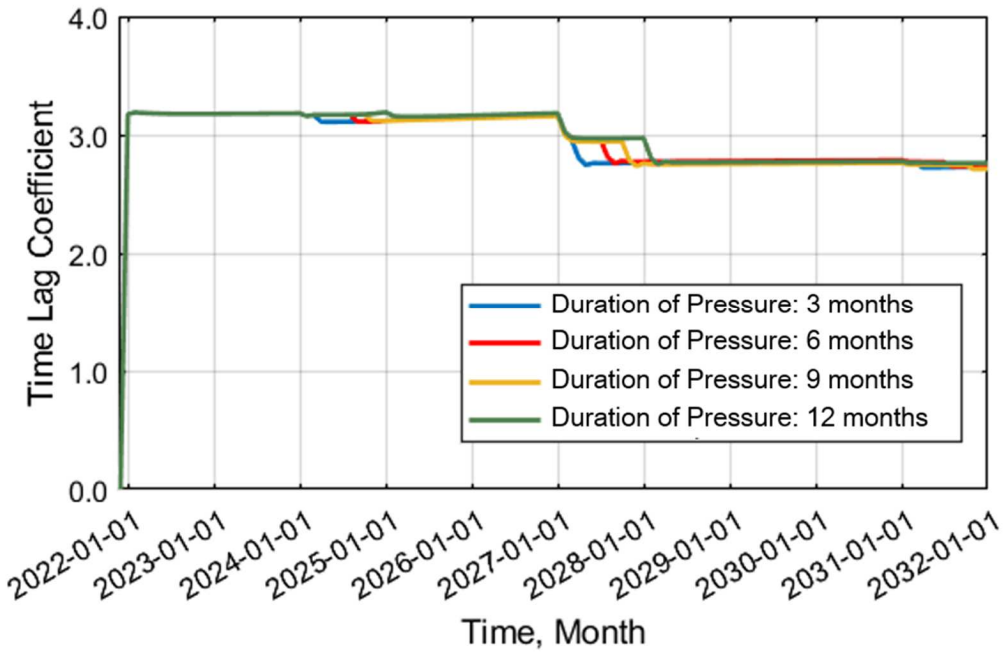


Figure 13. Variations in time-lag coefficients for different pressure impulse durations.

4.3.4. Injection Pressure Differential

After discussing the duration of the injection pressure impulse, the influence of the amplitude of injection pressure differential on inter-well connectivity is expounded in this part. The simulation results show that there is a positive correlation between injection pres-

sure differential and inter-well connectivity coefficient, suggesting that when the BHP of the producer remains unchanged, the higher the BHP, the higher the inter-well connectivity coefficient is (Figure 14). This may be because the increased injection pressure differential increases the ability to displace fluids and strengthens the force of fluid displacement in the reservoir, thus accelerating the exchange of oil–water phases between wells.

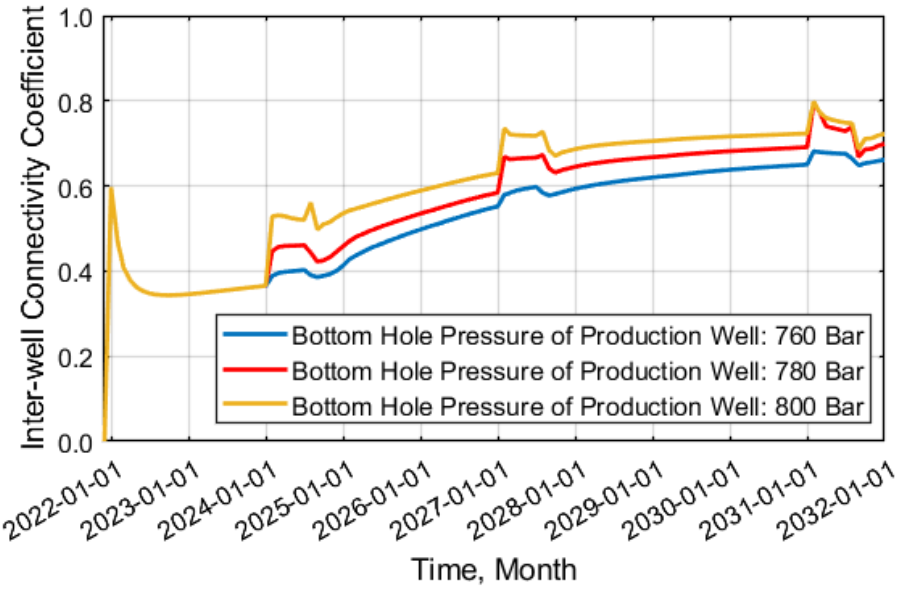


Figure 14. Inter-well connectivity coefficients under different injection pressure differentials.

Under different injection pressure differentials, the time-lag coefficients gradually decrease and stabilize (Figure 15). This means that over time, fluid transfer efficiency in the reservoir increases, and the impact of injection can be detected more quickly in the producer. With the increase in injector BHP, time-lag coefficients decrease obviously, indicating that the higher the injection pressure differential, the faster the ineffective circulation channels may be established and the more sensitive the fluid dynamic response.

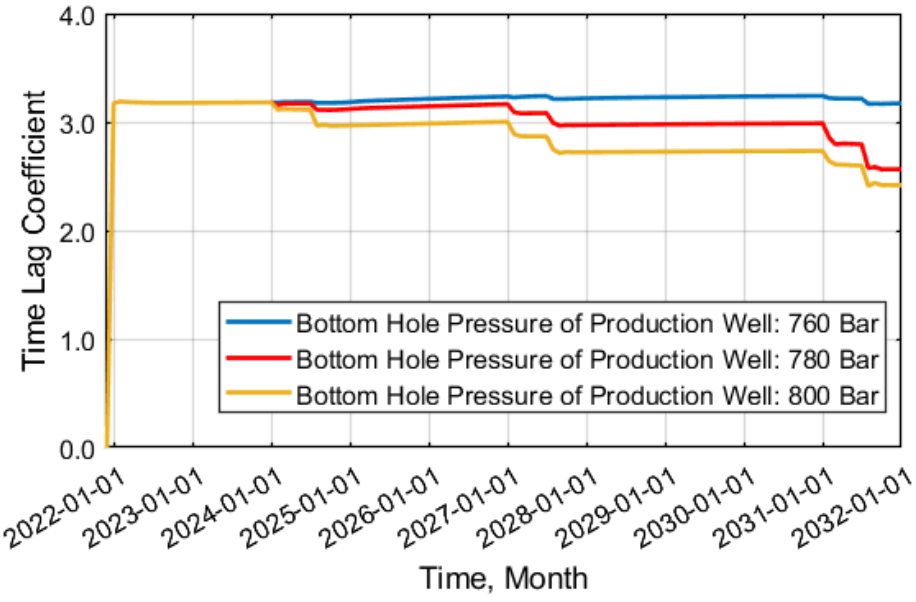


Figure 15. Variations in time-lag coefficients under different injection pressure differentials.

5. Multi-Well System Connectivity Analysis

The fluid flow pattern between multiple wells significantly differs from that of a single well pair. The complex injection-production conversion relationship between multiple wells often influences recovery efficiency and is of more practical guiding significance [45]. In a multi-well system, synergies and mutual interference may cause the characteristics of inter-well connectivity to differ greatly from those of the single-well model. The relationship between pressure differential and liquid yield becomes more implicit for different well groups. Two typical well configurations were considered: multi-producer–one-injector and one-injector-multi-producer, whose basic settings are presented in Table 4.

Table 4. Basic setting of inter-well connectivity analysis in two well group configurations.

Scenario	Well Pattern	Channel Permeability (mD)	Time of Commissioning (Month)	Well Spacing (m)
1	One-injector–four-producer	30, 60, 90, 120	120	212.15
2	Four-injector–one-producer	30, 60, 90, 120	120	212.15

5.1. Multi-Producer–One-Injector

A significant decrease in the inter-well connectivity coefficient has been observed in the multi-well system. The range of connectivity coefficient in the multi-well system decreases from 0–1 to 0–0.4 (Figure 16) compared to that of the single-well model (Figure 6). This may be attributed to the intensified interference/competition among wells. In a multi-producer–one-injector system, the fluid suffers more friction and pressure losses due to the greater number of wells involved as it flows from the injectors to the producers. These additional flow resistances would reduce the inter-well connectivity.

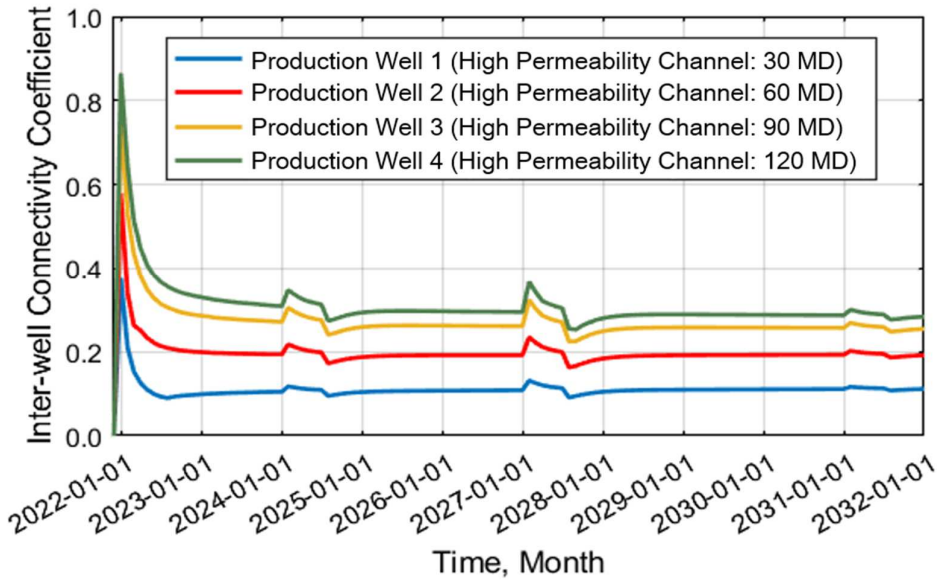
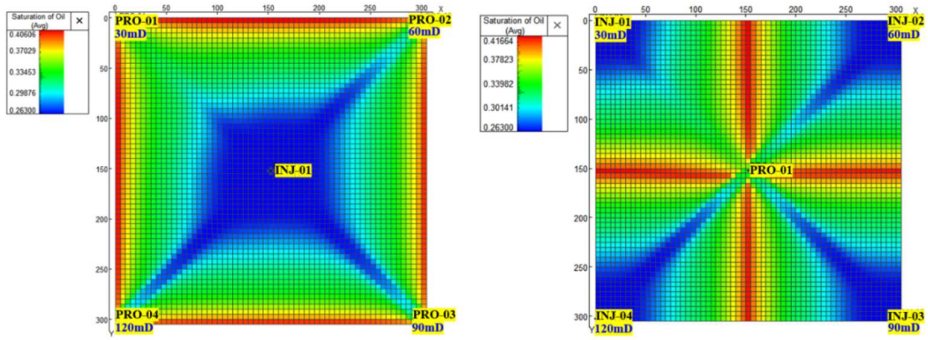


Figure 16. Inter-well connectivity coefficient in a multi-producer–one-injector model.

In addition, it is found that the inter-well connectivity coefficient for each of the four marginal injectors is different due to the pre-determined channel permeabilities. As the permeability increases from 30 mD to 120 mD, it is found that a higher channel permeability induces a larger inter-well connectivity coefficient, which follows the same pattern as that of a single-well model, which can be verified from the oil saturation distribution presented in Figure 17. The channel connected to the upper left corner has the lowest permeability (30 mD) against the matrix permeability (5 mD) and thus is characterized by non-obvious water migration in Figure 17a.



(a) **(b)**

Figure 17. Oil saturation distribution in (**a**) 4-producer–1-injector and (**b**) 4-injector–1-producer models.

As shown in Figure 18, the time-lag coefficients under different permeability channels remain relatively stable at the initial stage and change little over a longer period of time. This indicates that the connectivity between the injector and four producers is stable in the early stages. However, in 2017, the time-lag coefficient of each well experienced a certain decline. This may be due to an increase in injection pressure differential in 2017, which resulted in a fluid dynamics change affecting the time-lag coefficient. Generally, the time-lag coefficients in high permeability channels show a consistent trend, although the values differ slightly.

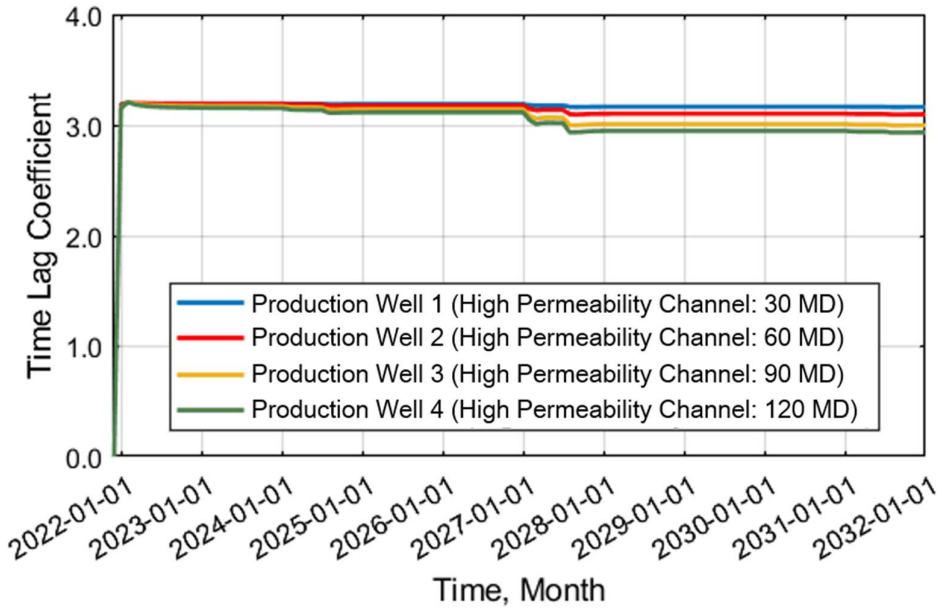


Figure 18. Time-lag coefficient in a multi-producer–one-injector model.

5.2. Multi-Injector–One-Producer

In order to achieve a better displacement effect and expand the sweep area during waterflood development, the well configuration adjustment between injectors and producers is often in high demand. Therefore, a four-injector–one-producer model was set up, in which the same five-point well pattern was applied with a central well converted into the production well.

Figure 19 shows the inter-well connectivity coefficients in a four-injector–one-producer system. The BHP of the four injectors remains the same throughout the run. It is observed that the inter-well connectivity coefficients in 1 January 2022–1 January 2027 are proportional to the permeability of the permeable channel, with the same pattern as that of the four-producer–one-injector system (Figure 17). However, from 1 January 2027 to 1 June

2027, the inter-well connectivity coefficients are inversely proportional to the permeability of the permeable channel: Injector 1 and Injector 2 are connected to the central producer with lower permeability, but they correspond to higher inter-well connectivity coefficients. This abnormal phenomenon might be related to the configuration of the well pattern and the intangible fluid passages.

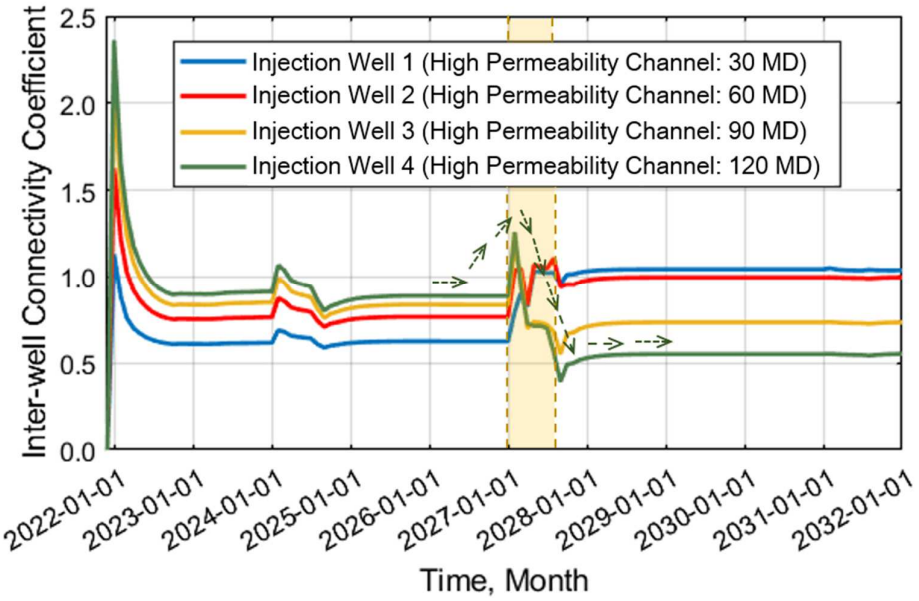


Figure 19. Inter-well connectivity coefficients in a multi-injector–one-producer model. The arrows indicate that the connectivity coefficients of injector 3 and injector 4 are reversed, despite their relatively high permeability channels.

Similarly, the time-lag coefficient also shows a reversal trend. Injector 4 has the channel of highest permeability, but its time-lag coefficient reverses to the maximum after 1 January 2027, as shown in Figure 20.

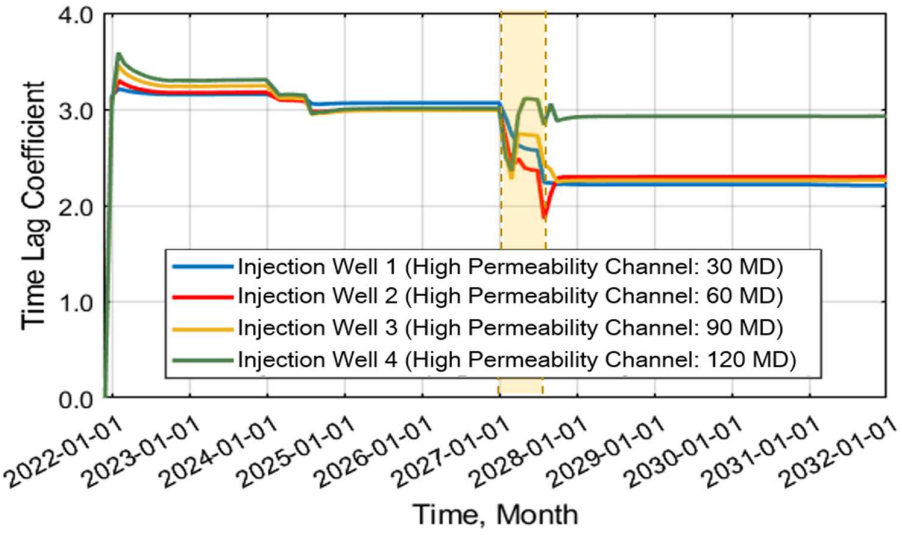


Figure 20. Time-lag coefficients in a multi-injector–one-producer model.

The analysis shows that for a four-producer–one-injector system, there are more producers than injectors, and increasing injection pressure differential may not cause significant pressure changes because the pressure fluctuations are mainly concentrated

around the single injector, while the BHP of the producer decreases as the result of continued production. Well group configuration determines the spatial distribution of water injected, which is more likely to form a strong pressure gradient in the reservoir and alter the fluid flow path, forming a new ineffective circulation channel. This may be the reason for the low connectivity coefficient of high permeability channels in the late simulation period.

6. Quantitative Classification of Ineffective Circulation Channels

The above discussions suggest that the ineffective circulation channels due to the change in injection pressure and the adjustment in production schedule profoundly impact the reservoir flow performance during waterflood development. To further identify the ineffective circulation channels quantitatively, this paper proposes the identification method of ineffective circulation channel level and takes the Qinhuangdao 32-6 Oilfield as an example to test its effect of practical application.

6.1. Rating of Ineffective Circulation Channels

The rating of ineffective circulation channels helps to identify the pairs of wells that require optimization and improve the production efficiency of the entire oilfield. Considering the inter-well connectivity coefficient, time-lag coefficient, and connectivity volume derived from the SV-DC model, a multidimensional score for evaluating well pair performance is proposed. As this is our initial exploration in this direction, the approach is intentionally kept simple. Based on the injection and production data from the Qinhuangdao 32-6 oilfield, which has a large number of well groups and sufficient data, the inter-well connectivity coefficient ranges from 0 to 1, the time-lag coefficient ranges from 0 to 5, and the connectivity volume ranges from 0 to 600,000 cubic meters.

$$\text{score} = \frac{mean_{\lambda} \times mean_{V}}{mean_{\tau}} \tag{29}$$

Using Equation (29), the level of ineffective circulation channels can be graded according to the calculated score. The classification criteria are established based on the distribution of these parameters and the experience from the Qinhuangdao 32-6 oilfield data analysis. The abundant data available allow us to compute a wide range of values, providing a solid foundation for defining the four levels of classification. The larger the inter-well connectivity coefficient and connectivity volume, and the smaller the time-lag coefficient, the higher the score, indicating better connectivity between wells. This scoring system divides the ineffective circulation channels into four levels, as shown in Table 5, with Level I representing the best connectivity and Level IV representing the poorest.

Table 5. Grading of ineffective circulation channels based on SV-DC model results. Levels I, II, III and IV indicate best, good, poor, and very poor connectivity, respectively.

Score	Level
score $\geq$ 20,000	I
10,000 $\leq$ score $\leq$ 20,000	II
5000 $\leq$ score $\leq$ 10,000	III
score $\leq$ 5000	IV

According to the proposed rating method, the development time and level of ineffective circulation channels in the entire oilfield are calculated as shown in Table 6. Well pairs of key optimization measures are selected to optimize the oilfield production strategy further. Due to the difficulty in determining the development time for ineffective circulation channels in Level III and Level IV well pairs, these cases are not displayed in Table 6. For the accuracy validation of the data in Table 6, reservoir engineering methods and tracer monitoring were considered. The development of ineffective circulation channels was determined and verified by tracer data collected in block NmI3. There are 25 wells

with strong connectivity identified by tracer monitoring results, of which 24 are consistent with the conclusion of our proposed identification of ineffective circulation channels, with an accuracy of 96%. For instance, in well group C03, well H03H had the earliest tracer breakthrough time, while well H19H1 had the latest. Correspondingly, the development of ineffective circulation channels in well group C03 and well H03H was also observed to be the earliest.

Table 6. Identification of ineffective channels in block Nm13, Qinhuangdao 32-6 Oilfield.

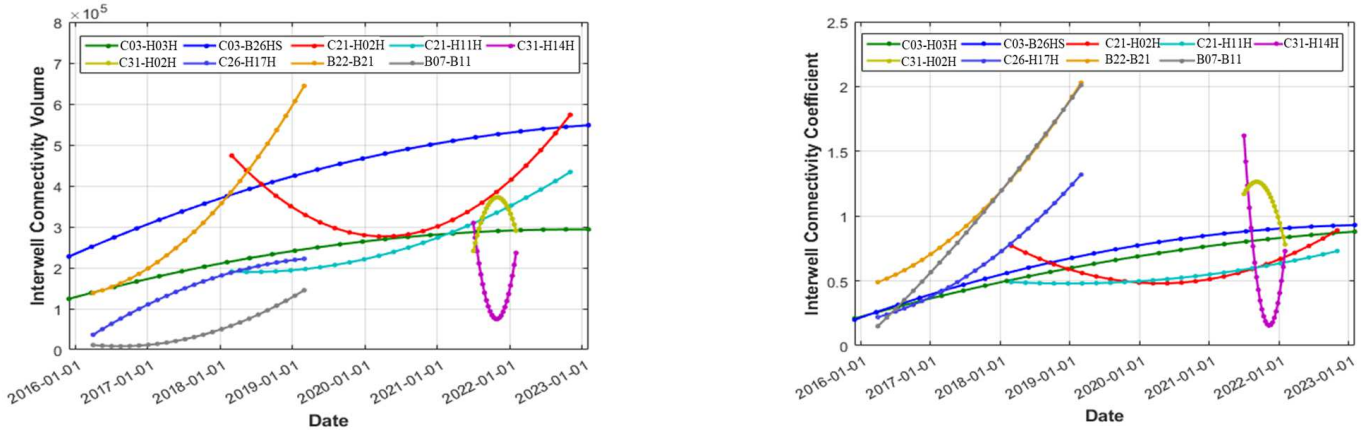
Well Group Name	Production Well	Development Time	Development Level	Well Group Name	Production Well	Development Time	Development Level
QHD32-6-C03	QHD32-6-H19H1	/	IV	QHD32-6-C15	QHD32-6-C11	August 2015	II
	QHD32-6-H21H	/	IV		QHD32-6-I43H	/	IV
	QHD32-6-H03H	June 2017	I	QHD32-6-C17	QHD32-6-I29H	/	IV
	QHD32-6-B26HS	May 2018	II		QHD32-6-I36H	/	IV
	QHD32-6-C02	/	IV		QHD32-6-C24	/	III
QHD32-6-C04	QHD32-6-C01	/	IV		QHD32-6-H14H	September 2017	II
	QHD32-6-D28H	/	IV	QHD32-6-C18	QHD32-6-I29H	/	IV
	QHD32-6-H1H2	/	III		QHD32-6-H14H	April 2019	I
	QHD32-6-H4H	/	IV	QHD32-6-C19	QHD32-6-I43H	/	IV
QHD32-6-C05	QHD32-6-H22H	/	IV		QHD32-6-H26H	/	IV
	QHD32-6-H1H2	September 2018	II	QHD32-6-C21	QHD32-6-H14H	July 2015	II
	QHD32-6-H4H	May 2018	II		QHD32-6-H2H	October 2016	I
	QHD32-6-I21H1	/	IV		QHD32-6-H12H2	/	IV
QHD32-6-C06	QHD32-6-H19H1	/	III	QHD32-6-C22	QHD32-6-H9H	January 2015	II
	QHD32-6-C2	/	IV		QHD32-6-H8H1	/	IV
	QHD32-6-H22H	July 2021	II		QHD32-6-H26H	/	III
	QHD32-6-I39H1	June 2021	II	QHD32-6-C25	QHD32-6-H2H	March 2015	II
	QHD32-6-I21H1	March 2019	II		QHD32-6-I22H	/	IV
QHD32-6-C07	QHD32-6-I39H1	January 2022	II		QHD32-6-C23	/	IV
	QHD32-6-H19H1	/	IV		QHD32-6-H11H	August 2018	I
	QHD32-6-H21H	January 2022	I	QHD32-6-C26	QHD32-6-H12H2	/	IV
	QHD32-6-I21H1	/	III		QHD32-6-C23	/	III
QHD32-6-C08	QHD32-6-H6H	November 2022	I		QHD32-6-H17H	January 2017	II
	QHD32-6-H21H	/	IV		QHD32-6-H9H	November 2016	II
QHD32-6-C09	QHD32-6-H15H1	June 2022	II	QHD32-6-C27	QHD32-6-H9H	/	IV
	QHD32-6-H1H2	/	IV		QHD32-6-H8H1	November 2022	I
	QHD32-6-H25H	/	IV		QHD32-6-H10H1	/	IV
QHD32-6-C10	QHD32-6-I21H1	/	IV	QHD32-6-C28	QHD32-6-H26H	December 2021	I
	QHD32-6-H1H2	/	IV		QHD32-6-I43H	/	IV
	QHD32-6-H25H	November 2022	II	QHD32-6-C29	QHD32-6-C2	/	IV

6.2. Application of Ineffective Circulation Channels

Thanks to the dynamic advantages of the SV-DC model, the connectivity level can be determined in combination with the recommended formulas, Equation (6) and Equation (12), and the data of connectivity coefficient, distribution coefficient (calculated based on the well group as a whole, where the total connectivity within the group is considered as 1, and individual well connectivity is derived as a proportion of this total), and connectivity volume from the early, middle and late stages can be obtained. The early stage refers to 0–40 months, the middle stage refers to 40–80 months, and the late stage refers to the subsequent 80 months. The well pairs classified as Level I and Level II in Table 6 are those with a high probability of developing ineffective circulation channels. Table 7 also focuses on discussing these well pairs in detail. In each of these stages, the inter-well connectivity coefficient, inter-well connected volume, and time-lag coefficient may vary

significantly. Notably, in some cases, the inter-well connectivity coefficient may exceed 1, which is generally due to the production rate being greater than the injection rate. This phenomenon is more likely to occur when there are high-permeability channels between the injection and production wells, leading to rapid response, or when there is a high injection pressure that induces a strong response in the surrounding production wells. Uneven pressure distribution and imbalance in injection-production configurations can also contribute to connectivity coefficients exceeding 1.

In order to further characterize the changing trend of connectivity parameters, various examples of well groups are listed in Table 8 according to the statistics of different curve forms. By plotting the inter-well connectivity volume and connectivity coefficient in the early, middle, and late stages of block Nml3 in the South Area, NmIII, and NmIV1 in the North Area, it is found that the curve can be subdivided into three forms: continuous rise, increase–decrease–increase and decrease–increase–decrease, as shown in Figure 21. The continuous rise category accounted for 58.8%, such as the well groups C03-H03H and C03-B26HS. The increase–decrease–increase category accounted for 19.7%, as well as groups C31-H14H and B21-B16. The decrease–increase–decrease category accounted for 21.5%, such as the C31-H02H and B21-B15. These classifications and examples help understand the dynamic variation characteristics and laws of connectivity volume of different well groups during waterflooding development.



(**a**) (**b**)

Figure 21. Variation trend of (**a**) inter-well connectivity volume and (**b**) inter-well connectivity coefficient in typical wells.

For well groups falling into the category of continuous rise, the development of ineffective circulation channels is significant, and the connectivity volume and connectivity coefficient are increasing. Maintaining a high connectivity volume and connectivity coefficient would help to improve reservoir recovery efficiency.

For wells H02H and H14H in well group C31, there is a trend of increase–decrease–increase. The connectivity volume and connectivity coefficient increase first, then decrease and rebound. Such patterns indicate that inter-well connectivity fluctuates over a period of time, possibly due to changes in injection-production conditions or geological factors. For such fluctuating trends, it is recommended to increase the injection rate during periods of decreased connectivity to stabilize inter-well connectivity. Additionally, more precise monitoring at the production well end is needed to assess the effectiveness of the adjustments. If necessary, dynamic regulation of injection pressure can be implemented to mitigate fluctuations and ensure a quick recovery of inter-well connectivity.

Table 7. Statistics of typical well groups in Qinhuangdao 32-6 oilfield.

Block	Well ID		Development Time	Development Parameters of Ineffective Circulation Channel								
				Connectivity Coefficient			Distribution Coefficient			Connectivity Volume (m^3)		
	Injection Well	Production Well		Early	Mid	Current	Early	Mid	Current	Early	Mid	Current
South Block NmI3	C03	H03H	June 2017	0.21	0.63	0.68	0.14	0.44	0.55	124,067	249,348	293,610
		B26HS	May 2018	0.20	0.81	0.83	0.11	0.46	0.60	227,385	438,899	548,067
	C25	H2H	March 2015	0.77	0.56	0.89	0.35	0.31	0.57	473,516	336,144	573,306
		H11H	August 2018	0.49	0.58	0.73	0.27	0.37	0.53	190,479	302,135	433,655
	C31	H14H	January 2015	1.62	0.29	0.73	0.61	0.11	0.28	309,358	85,684	236,323
		H2H	January 2015	1.17	1.25	0.78	0.37	0.39	0.24	240,949	365,040	290,403
North Block NmIII2	B12	B11	November 2017	0.72	0.82	1.21	0.26	0.30	0.44	71,276	79,329	119,762
	B22	B21	December 2021	1.23	2.16	1.76	0.24	0.42	0.34	471,031	1,162,740	538,428
North Block NmIV1	B16	B17	August 2016	0.22	0.83	1.32	0.093	0.35	0.56	36,503	192,496	221,955
		B21	August 2016	0.49	1.34	2.03	0.127	0.347	0.526	138,368	405,413	644,107
		B11	April 2016	0.15	1.35	2.01	0.043	0.385	0.573	11,156	64,637	145,147

Table 8. Statistics of the change in connectivity volume in Qinhuangdao 32-6 oilfield.

Tracing Pattern	Proportion of the Number of Injector-Producer	Typical Well
Increase–decrease–increase	19.7%	C31-H14H; B21-B16
Decrease–increase–decrease	21.5%	C31-H02H; B21-B15
Continuous rise	58.8%	C03-H03H; C03-B26HS

The decrease–increase–decrease pattern has been witnessed in wells C31-H02H and B21-B15. The connectivity volume and coefficient first decrease, then increase, and finally decrease. Such patterns may reflect changes in the dominant water flow path, indicating periodic development of ineffective circulation channels. Compared with the first two patterns, the connectivity changes in this pattern are more complex. For such complex periodic changes, it is recommended to optimize the injection rate during the phases of decreasing connectivity to maintain a stable inter-well connection. Phase-wise adjustments to both injection pressure and production rate can help maintain balanced pressure between well groups, reducing the further development of ineffective circulation channels. Regular evaluations of inter-well connectivity are also advised to assess the effectiveness of injection and production adjustments.

In summary, the proposed SV-DC model associated with the recommended grading formula can be used to analyze the dynamic changes in inter-well connectivity parameters, which can identify and understand the evolution law of connectivity volume and connectivity coefficients of different well groups, which is of great significance for optimizing water injection strategy and improving reservoir recovery efficiency. Compared with conventional methods, the SV-DC model provides a more flexible approach to handle the dynamic changes in inter-well connectivity, especially under complex injection and production conditions. Unlike traditional methods that excel in stability and simplicity, the SV-DC model captures the dynamic characteristics of inter-well connectivity with higher time resolution, enabling more detailed analysis across different injection phases. These features make the SV-DC model advantageous in guiding future injection strategies and improving recovery efficiency.

The algorithm model for calculating the inter-well connectivity coefficient and the quantitative evaluation methods for ineffective circulation channels can be easily programmed into the oil reservoir development information system platform to serve field operators. This approach is highly advantageous as it enables dynamic identification of relevant parameters, providing updated values at each time step, which facilitates real-time monitoring and improves decision-making accuracy in reservoir management. The corresponding technical route has considerable guiding significance for the engineering background involving injection wells and production wells, such as geothermal resources exploitation, surface drilling, and extraction of coalbed methane wells and carbon dioxide underground storage. However, the method also has certain limitations, primarily in terms of data requirements. The method requires input data to be continuous and uninterrupted, which can present challenges in certain special cases in the field, such as well shut-in operations. Under these circumstances, the model may struggle to accurately identify dynamic parameters. Addressing these challenges will be a key focus of our future work.

7. Conclusions

In this paper, a state variable-based dynamic capacitance model (SV-DC model) has been established to analyze the inter-well connectivity and its influencing factors of single-well systems and multi-well systems. The main conclusions are as follows:

(1) The proposed innovative SV-DC model, enhanced with intelligent algorithms, combines dynamic data and geological features to more accurately identify inter-well connectivity and its evolution. By leveraging AI-driven techniques, the SV-DC model significantly improves the interpretation of complex fluid transfer patterns between

wells/well groups, surpassing traditional static and dynamic analysis methods in capturing dynamic characteristics and providing more precise and adaptive insights.

(2) The dynamic changes in injection rate and liquid production rate were deeply studied, and the sensitivity analyses of permeability, permeable channel width, injection pressure differential, and duration were carried out. The results show that higher permeability, wider permeable channels, and longer injection pressure maintenance can significantly enhance inter-well connectivity coefficients and reduce time-lag coefficients.

(3) The production performance analysis of the multi-well system was carried out, including two well group configurations of four-producer–one-injector and four-injector–one-producer. It is found that inter-well connectivity in multi-well systems is significantly affected by well-group configuration and inter-well interference effects. The four-injector–one-producer system shows high connectivity and low time lag for the high-permeability channel. In contrast, for the four-producer–one-injector system, there is an abnormal situation of low inter-well connectivity, which is speculated to be a symptom of the formation of ineffective circulation channels.

(4) By applying the SV-DC model, the dynamic changes in inter-well connectivity coefficient and connectivity volume were analyzed, and the connectivity levels of ineffective circulation channels were divided according to the changes. The results show three typical change patterns of the development of ineffective circulation channels. These change patterns provide an important basis for optimizing oil fields' injection and production strategy and contribute to improving oil recovery.

In conclusion, through systematic numerical simulation and model verification, this study reveals the dynamic characteristics and influencing factors of inter-well connectivity, providing important theoretical support and practical guidance for oilfield development. This algorithm model can be used to calculate the inter-well connectivity coefficient and as a quantitative evaluation method for ineffective circulation channels. It can be conveniently programmed into the reservoir development system platform to serve field operators. This method has obvious advantages because it can dynamically identify relevant parameters and provide updated values at each time step, thus achieving real-time monitoring and improving the accuracy of oil reservoir management decisions.

Author Contributions: Methodology, L.G., S.W., Z.K., S.D. and X.Y.; Software, L.G., S.W., Z.K. and M.Z.; Validation, L.G., S.W., Z.K., S.D. and X.Y.; Formal analysis, L.G. and X.Y.; Investigation, L.G., Haitong Yang and M.Z.; Resources, H.Y. and M.Z.; Data curation, L.G., X.Y. and M.Z.; Writing–original draft, L.G.; Writing–review & editing, L.G.; Supervision, S.W., Z.K. and S.D.; Project administration, S.W. All authors have read and agreed to the published version of the manuscript.

Funding: This research was funded by the National Natural Science Foundation of China under the project 'Study and Application of Permeation Mechanics in Enhanced Oil Recovery in High Permeability and High Water-Cut Thin Oil Reservoirs' (Grant No. 52374051).

Institutional Review Board Statement: Not applicable.

Informed Consent Statement: Not applicable.

Data Availability Statement: The data presented in this study are available on request.

Conflicts of Interest: The authors declare no conflict of interest.

References

1. Dong, C.; Zhang, B.; Yang, E.; Lu, J.; Zhang, L. Identification of Water Flooding Advantage Seepage Channels Based on Meta-Learning. *Energies* **2023**, *16*, 687. [CrossRef]
2. Zhou, W.; Cao, Z.; Zhang, Y.; Wang, D. Research on Identification and Control of Dominant Seepage Channels in Medium and Low Permeability Reservoirs. In *Proceedings of the International Field Exploration and Development Conference 2023*; Zhao, D., Ed.; Springer Nature: Singapore, 2024; pp. 588–598. [CrossRef]
3. Zheng, Q.; Liu, H.; Zhang, B.; Li, N.; Li, F. Identification of high permeability channels along horizontal wellbore in heterogeneous reservoir with bottom water. *J. Pet. Explor. Prod. Technol.* **2014**, *4*, 309–314. [CrossRef]

4. Lei, Q.; Weng, D.; Luo, J.; Zhang, J.; Li, Y.; Wang, X.; Guan, B. Achievements and Future Work of Oil and Gas Production Engineering of CNPC. *Pet. Explor. Dev.* **2019**, *46*, 145–152. [CrossRef]
5. Zhao, S.T.; Li, Q.; He, X.R.; Song, K.P.; Zhang, J.C. Investigation on Circulating Path of Injected Water for High Water-Cut Oilfield. *Adv. Mater. Res.* **2015**, *1073*, 2201–2204. [CrossRef]
6. Li, G.; Song, X.; Tian, S.; Zhu, Z. Intelligent Drilling and Completion: A Review. *Engineering* **2022**, *18*, 33–48. [CrossRef]
7. Yin, X.; Guo, J.-H.; Sun, L.; Wei, L.; Wang, Y.; Wang, Z.; Wang, H. Quantification of Ineffective Water Circulation in Thick Reservoir Based on Machine Learning. In *Proceedings of the International Field Exploration and Development Conference 2021*; Lin, J., Ed.; Springer Nature: Singapore, 2022; pp. 5196–5204. [CrossRef]
8. Li, H. Study on the limit of ineffective cycle control in Lamadian Oilfield in the late period of ultra-high water cut. *E3S Web Conf.* **2024**, *528*, 01007. [CrossRef]
9. Li, C.-X.; Liu, M.; Guo, B.-C. Classification of tight sandstone reservoirs based on NMR logging. *Appl. Geophys.* **2019**, *16*, 549–558. [CrossRef]
10. Liang, H.; Wu, M.; Wang, J. Well test analysis method for CO_2 content gas reservoirs of Ying-Qiong Basin. *IOP Conf. Ser. Earth Environ. Sci.* **2019**, *252*, 052003. [CrossRef]
11. Lin, J.; He, H.; Wang, Y. A well test analysis model of generalized tube flow and seepage coupling. *Pet. Explor. Dev.* **2021**, *48*, 923–934. [CrossRef]
12. Gutiérrez Sama, S.; Farenc, M.; Barrère-Mangote, C.; Lobinski, R.; Afonso, C.; Bouyssière, B.; Giusti, P. Molecular Fingerprints and Speciation of Crude Oils and Heavy Fractions Revealed by Molecular and Elemental Mass Spectrometry: Keystone between Petroleomics, Metallopetroleomics, and Petrointeractomics. *Energy Fuels* **2018**, *32*, 4593–4605. [CrossRef]
13. Dessirier, B.; Sharma, K.M.; Pedersen, J.; Tsang, C.-F.; Niemi, A. Channel Network Modeling of Flow and Transport in Fractured Rock at the Äspö HRL: Data-Worth Analysis for Model Development, Calibration and Prediction. *Water Resour. Res.* **2023**, *59*, e2022WR033816. [CrossRef]
14. Xu, R.; Yan, T.; Han, X.; Qu, J.; Feng, J. Mass Transfer Analysis of CO_2-Water-Rock Geochemical Reactions in Reservoirs. *Energies* **2023**, *16*, 5862. [CrossRef]
15. Cui, W.; Yang, W.; Jing, C.; Wang, Y. Research on Identification Method of Dominant Seepage Flow Channel of Fractured Horizontal Wells in Tight Oil Reservoir Based on Fuzzy Synthetic Evaluation Model. In *Proceedings of the International Field Exploration and Development Conference 2018*; Lin, J., Ed.; Springer: Singapore, 2020; pp. 2007–2024. [CrossRef]
16. James, R.; Amasi, A.I.; Wynants, M.; Nobert, J.; Mtei, K.M.; Njau, K. Tracing the dominant sources of sediment flowing towards Lake Victoria using geochemical tracers and a Bayesian mixing model. *J. Soils Sediments* **2023**, *23*, 1568–1580. [CrossRef]
17. Du, S.-Y.; Zhao, X.-G.; Xie, C.-Y.; Zhu, J.-W.; Wang, J.-L.; Yang, J.-S.; Song, H.-Q. Data-driven production optimization using particle swarm algorithm based on the ensemble-learning proxy model. *Pet. Sci.* **2023**, *20*, 2951–2966. [CrossRef]
18. Jing, C.; Dong, X.; Cui, W.; Dong, Z.; Ren, L.; Gu, X.; He, Y.; Pu, C.; Liu, X. Artificial neural network–based time-domain interwell tracer testing for ultralow-permeability fractured reservoirs. *J. Pet. Sci. Eng.* **2020**, *195*, 107558. [CrossRef]
19. Li, W.; Yang, J. Research and Application of Low Efficiency and Invalid Circulation Field Quantitative Identification Method. In *Proceedings of the International Field Exploration and Development Conference 2021*; Lin, J., Ed.; Springer Nature: Singapore, 2022; pp. 3045–3053.
20. Yousef, A.A.; Gentil, P.; Jensen, J.L.; Lake, L.W. A Capacitance Model To Infer Interwell Connectivity From Production- and Injection-Rate Fluctuations. *SPE Reserv. Eval. Eng.* **2006**, *9*, 630–646. [CrossRef]
21. Sayarpour, M.; Kabir, C.S.; Lake, L.W. Field Applications of Capacitance-Resistance Models in Waterfloods. *SPE Reserv. Eval. Eng.* **2009**, *12*, 853–864. [CrossRef]
22. Kim, J.S. *Development of Linear Capacitance–Resistance Models for Characterizing Waterflooded Reservoir*; University of Texas: Austin, TX, USA, 2011. [CrossRef]
23. Salehian, M.; Soleimani, R. Development of Integrated Capacitance Resistive Model for Predicting Waterflood Performance: A Study on Formation Damage. *Energy Sources Part A Recovery Util. Environ. Eff.* **2018**, *40*, 1814–1825. [CrossRef]
24. Mamghaderi, A.; Pourafshary, P. Water flooding performance prediction in layered reservoirs using improved capacitance-resistive model. *J. Pet. Sci. Eng.* **2013**, *108*, 107–117. [CrossRef]
25. Zhang, Z.; Li, H.; Zhang, D. Water flooding performance prediction by multi-layer capacitance-resistive models combined with the ensemble Kalman filter. *J. Pet. Sci. Eng.* **2015**, *127*, 1–19. [CrossRef]
26. Zhang, Z.; Li, H.; Zhang, D. Reservoir characterization and production optimization using the ensemble-based optimization method and multi-layer capacitance-resistive models. *J. Pet. Sci. Eng.* **2017**, *156*, 633–653. [CrossRef]
27. Prakasa, B.; Shi, X.; Muradov, K.; Davies, D. Novel Application of Capacitance-Resistance Model for Reservoir Characterisation and Zonal, Intelligent Well Control. In Proceedings of the SPE/IATMI Asia Pacific Oil & Gas Conference and Exhibition, Jakarta, Indonesia, 17–19 October 2017; OnePetro: Richardson, TX, USA, 2017. [CrossRef]
28. Temizel, C.; Salehian, M.; Cinar, M.; Gok, I.M.; Alklih, M.Y. A Theoretical and Practical Comparison of Capacitance-Resistance Modeling with Application to Mature Fields. In Proceedings of the SPE Kingdom of Saudi Arabia Annual Technical Symposium and Exhibition, Dammam, Saudi Arabia, 23–26 April 2018; OnePetro: Richardson, TX, USA, 2018. [CrossRef]
29. Ghamdi, A.A.A.; Opoku, D.; Awotunde, A.; Mahmoud, M.; Liao, Q. Optimization of Waterflooding Utilizing Data Driven Models: An Application of the Two-Phase Capacitance Resistance Model. In Proceedings of the SPE Europec Featured at 82nd EAGE Conference and Exhibition, Amsterdam, The Netherlands, 18–21 October 2021; OnePetro: Richardson, TX, USA, 2021. [CrossRef]

30. Davudov, D.; Malkov, A.; Venkatraman, A. Integration of Capacitance Resistance Model with Reservoir Simulation. In Proceedings of the SPE Improved Oil Recovery Conference, Virtual, 31 August–4 September 2020; OnePetro: Richardson, TX, USA, 2020. [CrossRef]
31. Lesan, A.; Shams, R.; Pourafshary, P.; Bahrodi, A.; Rastkerdar, H. Application of the modified capacitance-resistance method to model reservoir pressure maintenance. *Results Eng.* **2023**, *19*, 101231. [CrossRef]
32. Parra, J.E.; Samaniego, V.F.; Lake, L.W. Application of the Producer-Based Capacitance Resistance Model to Undersaturated Oil Reservoirs in Primary Recovery. *SPE J.* **2023**, *28*, 2256–2273. [CrossRef]
33. Parra, J.E.; Samaniego, V.F.; Lake, L.W. CRM-Aquifer-Fractional Flow Model to Characterize Oil Reservoirs with Natural Water Influx. *SPE J.* **2024**, *29*, 538–553. [CrossRef]
34. Kang, Z.J.; Zhao, H.; Zhang, H.; Zhang, Y.; Li, Y.; Sun, H.T. Research on Applied Mechanics with Reservoir Interwell Dynamic Connectivity Model and Inversion Method in Case of Shut-In Wells. *Appl. Mech. Mater.* **2014**, *540*, 296–301. [CrossRef]
35. Zhao, H.; Yao, J.; Lue, A.-M.; Wang, W. Reservoir interwell dynamic connectivity inversion based on injection and production data. *Zhongguo Shi You Daxue Xuebao/J. China Univ. Pet. Ed. Nat. Sci.* **2010**, *34*, 91–94.
36. Liu, F.; Mendel, J.M.; Nejad, A.M. Forecasting Injector/Producer Relationships from Production and Injection Rates Using an Extended Kalman Filter. *SPE J.* **2009**, *14*, 653–664. [CrossRef]
37. Mendel, J.M. Fuzzy logic systems for engineering: A tutorial. *Proc. IEEE* **1995**, *83*, 345–377. [CrossRef]
38. Zhai, D.; Mendel, J.M.; Liu, F. A New Method for Continual Forecasting of Interwell Connectivity in Waterfloods Using an Extended Kalman Filter. In Proceedings of the SPE Western Regional Meeting, San Jose, CA, USA, 24–26 March 2009; OnePetro: Richardson, TX, USA, 2009. [CrossRef]
39. Zhai, D.; Mendel, J.M. An Inequality-Constrained Extended Kalman Filter for Continual Forecasting of Interwell Connectivities in Waterfloods. In Proceedings of the SPE Western Regional Meeting, Anaheim, CA, USA, 27–29 May 2010; OnePetro: Richardson, TX, USA, 2010. [CrossRef]
40. Du, X.; Cheng, L.; Chen, J.; Cai, J.; Niu, L.; Cao, R. Numerical Investigation for Three-Dimensional Multiscale Fracture Networks Based on a Coupled Hybrid Model. *Energies* **2021**, *14*, 6354. [CrossRef]
41. Tang, B.; Ren, K.; Lu, H.; Li, C.; Geng, C.; Wei, L.; Chai, Z.; Wu, S. Study on Residual Oil Distribution Law during the Depletion Production and Water Flooding Stages in the Fault-Karst Carbonate Reservoirs. *Processes* **2023**, *11*, 2147. [CrossRef]
42. Wu, Y.; Zhang, Y.; Wang, J.; Ma, Y.; Song, Z.; Zeng, X.; Cao, A. Study on the mechanism of improved oil recovery by nitrogen foam flooding in bottom water reservoirs. *Front. Energy Res.* **2023**, *11*, 1120635. [CrossRef]
43. Zhou, Y.; Lei, S.; Du, X.; Ju, S.; Li, W. Injection-production optimization of carbonate reservoir based on an inter-well connectivity model. *Energy Explor. Exploit.* **2021**, *39*, 1666–1684. [CrossRef]
44. Nalasavagan, K.; bin Abdul Rahman, H.; bin Azman, M.F.; bin Bakar, R. Managing Accelerated Water Breakthrough in High Permeability Contrast Waterflood Reservoirs, and Achieving Production Conformance Through Injection Redistribution Strategy. In Proceedings of the ADIPEC, Abu Dhabi, United Arab Emirates, 31 October–3 November 2022; p. D012S139R003. [CrossRef]
45. Hao, T.; Zhong, L.; Liu, J.; Zhang, X.; Zhang, L. Waterflood Efficiency Assessment Using Injection–Production Relationship Analysis Method. *Math. Geosci.* **2023**, *55*, 201–228. [CrossRef]

Disclaimer/Publisher's Note: The statements, opinions and data contained in all publications are solely those of the individual author(s) and contributor(s) and not of MDPI and/or the editor(s). MDPI and/or the editor(s) disclaim responsibility for any injury to people or property resulting from any ideas, methods, instructions or products referred to in the content.